Advances in Water Resources 142 (2020) 103620

Contents lists available at ScienceDirect

Advances in Water Resources

journal homepage: www.elsevier.com/locate/advwatres

Flow in porous media with low dimensional fractures by employing enriched Galerkin method

T. Kadeethum [a], H.M. Nick [a,b,*], S. Lee [c], F. Ballarin [d]

[a] Technical University of Denmark, Denmark
[b] Delft University of Technology, the Netherlands
[c] Florida State University, Florida, USA
[d] mathLab, Mathematics Area, SISSA, Italy

ARTICLE INFO

Keywords:
Fractured porous media
Mixed-dimensional
Enriched Galerkin
Finite element method
Heterogeneity
Local mass conservative

ABSTRACT

This paper presents the enriched Galerkin discretization for modeling fluid flow in fractured porous media using the mixed-dimensional approach. The proposed method has been tested against published benchmarks. Since fracture and porous media discontinuities can significantly influence single- and multi-phase fluid flow, the heterogeneous and anisotropic matrix permeability setting is utilized to assess the enriched Galerkin performance in handling the discontinuity within the matrix domain and between the matrix and fracture domains. Our results illustrate that the enriched Galerkin method has the same advantages as the discontinuous Galerkin method; for example, it conserves local and global fluid mass, captures the pressure discontinuity, and provides the optimal error convergence rate. However, the enriched Galerkin method requires much fewer degrees of freedom than the discontinuous Galerkin method in its classical form. The pressure solutions produced by both methods are similar regardless of the conductive or non-conductive fractures or heterogeneity in matrix permeability. This analysis shows that the enriched Galerkin scheme reduces the computational costs while offering the same accuracy as the discontinuous Galerkin so that it can be applied for large-scale flow problems. Furthermore, the results of a time-dependent problem for a three-dimensional geometry reveal the value of correctly capturing the discontinuities as barriers or highly-conductive fractures.

1. Introduction

Modeling of fluid flow in fractured porous media is essential for a wide variety of applications including water resource management (Glaser et al., 2017; Peng et al., 2017), geothermal energy (Willems and Nick, 2019; Salimzadeh et al., 2019a; Salimzadeh and Nick, 2019), oil and gas (Wheeler et al., 2019; Kadeethum et al., 2019c; Andrianov and Nick, 2019; Kadeethum et al., 2020c), induced seismicity (Rinaldi and Rutqvist, 2019), CO_2 sequestration (Salimzadeh et al., 2018), and biomedical engineering (Vinje et al., 2018; Ruiz Baier et al., 2019; Kadeethum et al., 2020a). A fractured porous medium can be decomposed into the bulk matrix and fracture domains, which are generally anisotropic, heterogeneous, and have substantially discontinuous material properties that can span several orders of magnitude (Matthai and Nick, 2009; Flemisch et al., 2018; Jia et al., 2017; Bisdom et al., 2016). These discontinuities can critically enhance or hinder the flux within and between the bulk matrix and fracture domains. Accurately capturing the flow behavior controlled by these discontinuities in complex media is still challenging (Nick and Matthai, 2011a; De Dreuzy et al., 2013; Flemisch et al., 2016; Hoteit and Firoozabadi, 2008; Zhang et al., 2016).

There are two main approaches to represent the fluid flow between the matrix and fracture domain (Nick and Matthai, 2011b; Flemisch et al., 2018; Juanes et al., 2002). The first model, an equi-dimensional model, discretizes the matrix and fracture domain with same dimensionality (Salinas et al., 2018). This approach is straightforward to implement, and no coupling condition is required. This approach is utilized to model, for example, coupled hydromechanical of fractured rocks using the finite-discrete element method (Latham et al., 2013; 2018), and can also capture fracture propagation using an immersed-body method (Obeysekara et al., 2018) or phase-field approach (Santillan et al., 2018; Lee et al., 2016b; 2018). The second model, which we call a mixed-dimensional model hereafter, reduces the fracture domain to a lower dimensionality by assuming the fracture thickness is much smaller com-

* corresponding author at: Technical University of Denmark, Lyngby, Denmark, Delft University of Technology, The Netherlands.
E-mail addresses: teekad@dtu.dk (T. Kadeethum), h.m.nick@tudelft.nl (H.M. Nick), lee@math.fsu.edu (S. Lee), francesco.ballarin@sissa.it (F. Ballarin).

https://doi.org/10.1016/j.advwatres.2020.103620
Received 21 December 2019; Received in revised form 6 May 2020; Accepted 10 May 2020
Available online 31 May 2020

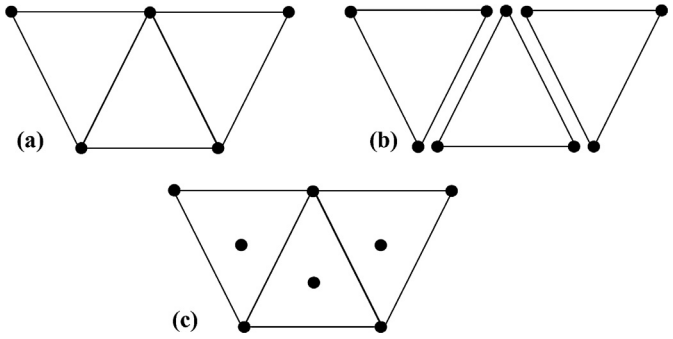

Fig. 1. Comparison of degrees of freedom for linear polynomial case among (**a**) continuous Galerkin (CG), (**b**) discontinuous Galerkin (DG), and (**c**) enriched Galerkin (EG) function spaces.

pared to the size of matrix domain (Boon et al., 2018; Martin et al., 2005; Berrone et al., 2018). The second approach has several benefits; for example, it reduces the degrees of freedom (DOF) (Nick and Matthai, 2011a) as the fracture domain is represented as the interface, which is part of the matrix domain, and subsequently, this approach can improve mesh quality (reduce the mesh skewness) (Matthai et al., 2010). Since the fractures are interfaces, one can use a larger mesh size, which satisfies Courant-Friedrichs-Lewy (CFL) condition more easily (Juanes et al., 2002; Nick and Matthai, 2011b).

In the past decades, many approaches have been proposed to model the fractured porous media using the mixed-dimensional approach; (1) two-point flux approximation in unstructured control volume finite-difference technique (Karimi-Fard et al., 2004), (2) multi-point flux approximation using mixed finite element method on general quadrilateral and hexahedral grids (Wheeler et al., 2012), (3) eXtended finite element combined with mixed finite element formulation (D'Angelo and Scotti, 2012; Prevost and Sukumar, 2016; Sanborn and Prevost, 2011), (4) embedded discrete fracture-matrix (DFM) modeling with non-conforming mesh (Hajibeygi et al., 2011; Odsaeter et al., 2019), (5) mixed approximation such as mimetic finite difference (Flemisch and Helmig, 2008; Formaggia et al., 2018), (6) two-field formulation using mixed finite element (MFE) (Martin et al., 2005; Fumagalli et al., 2019), and (7) disconinuous Galerkin (DG) method (Rivie et al., 2000; Hoteit and Firoozabadi, 2008; Antonietti et al., 2019; Arnold et al., 2002).

We focus on the finite element based discretization such as the DG and MFE methods that ensure the local mass conservative property. Moreover, they are flexible enough to discretize complex subsurface geometries such as intersections of fractures or irregular-shaped matrix blocks. Additionally, the aforementioned methods are capable of mimicking the fracture propagation in poroelastic media using either cohesive zone method or linear elastic fracture mechanics framework (Salimzadeh and Khalili, 2015; Salimzadeh et al., 2019b; Secchi and Schrefler, 2012; Segura and Carol, 2008). However, the MFE method requires an additional primary variable (fluid velocity) which may require more computational resources, especially in a three-dimensional

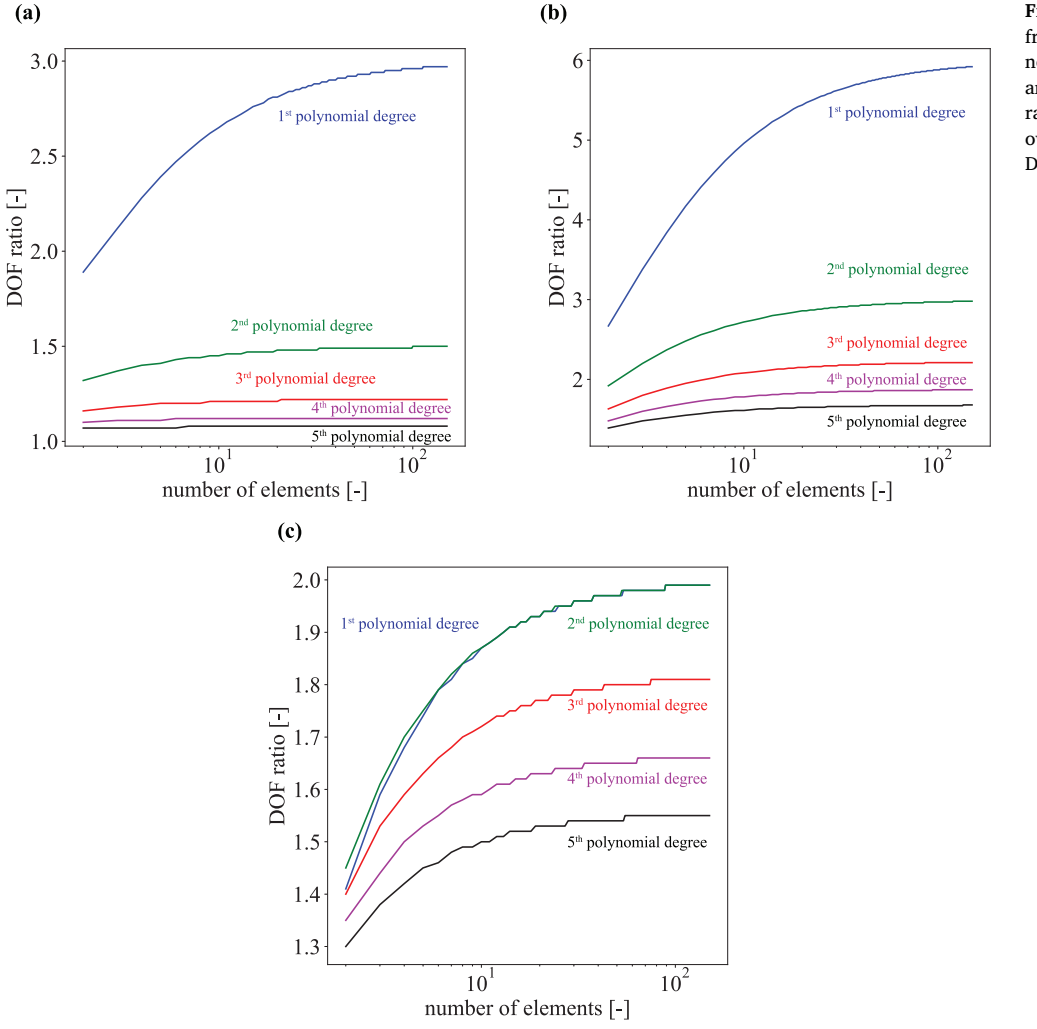

Fig. 2. Comparison of ratio of degrees of freedom for 1st, 2nd, 3rd, 4th, and 5th polynomial degree cases on triangular element among CG, EG, and DG discretizations: (**a**) ratio of EG over CG DOF, (**b**) ratio of DG over CG DOF, and (**c**) ratio of DG over EG DOF.

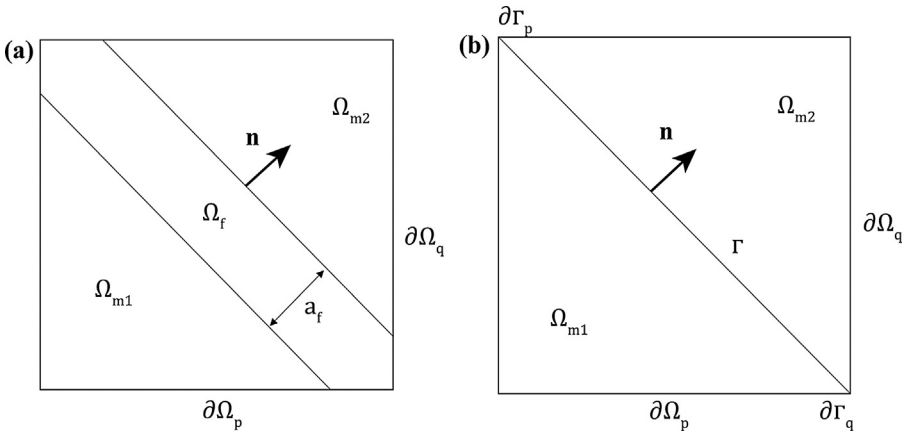

Fig. 3. Illustration of (**a**) equi-dimensional and (**b**) mixed-dimensional settings. Note that these illustrations are the graphical representations; in the numerical model $\partial\Omega_p$, $\partial\Omega_q$, $\partial\Gamma_p$, or $\partial\Gamma_q$ have to be imposed on all boundary faces of each domain.

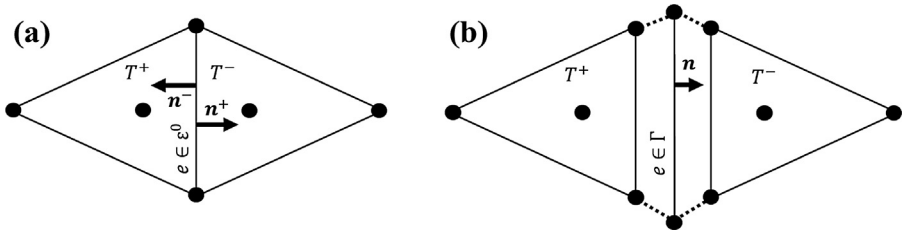

Fig. 4. Illustration of EG elements (**a**) without fracture interface and (**b**) with fracture interface.

domain Kadeethum et al. (2019a). Mesh adaptivity is also not straightforward to implement Lee and Wheeler (2017), and it requires the inversion of the permeability tensor, which may lead to an ill-posed problem (Choo and Lee, 2018). The DG method also can be considered as a computationally expensive method as it requires a large number of DOF (Sun and Liu, 2009; Lee et al., 2016a).

To resolve some of the shortcomings mentioned above, we propose an enriched Galerkin (EG) discretization (Lee et al., 2016a; Zi et al., 2004; Khoei et al., 2018) to model fluid flow in fractured porous media using the mixed-dimensional approach. The EG method, utilized in this study, composes of the CG function space augmented by a piecewise-constant function at the center of each element. This method has the same interior penalty type bilinear form as the DG method (Sun and Liu, 2009; Lee et al., 2016a). The EG method, however, only requires to have discontinuous constants as illustrated in Fig. 1, so it has fewer DOF than the DG method. Fig. 2 presents the comparison of the DOF ratio among CG, EG, and DG methods, and it shows that the EG method requires half of the DOF needed by the DG method (triangular elements with the first polynomial degree approximation). Note that this ratio decreases as the polynomial degree approximation increase. The EG method has been developed to solve general elliptic and parabolic problems with dynamic mesh adaptivity (Lee and Wheeler, 2017; 2018; Lee et al., 2018) and extended to address the multiphase fluid flow problems (Lee and Wheeler, 2018). Recently, the EG method has been also applied to solve the non-linear poroelastic problem (Choo and Lee, 2018; Kadeethum et al., 2019b; 2020b), and compared its performance with other two- and three-field formulation methods (Kadeethum et al., 2019a). To the best of our knowledge, this is the first attempt to apply the EG discretization in the mixed-dimensional setting.

The rest of the paper is organized as follows. The methodology section includes model description, mathematical equations, and their discretizations for the EG and DG methods. Subsequently, the block structure used to compose the EG function space and the coupling terms between matrix and fracture domains is illustrated. The numerical examples section presents five examples, and the conclusion is finally provided.

2. Methodology

2.1. Governing equations

We first briefly introduce the equi-dimensional model, which is used to derive the mixed-dimensional model. We are interested in solving steady-state and time-dependent single phase fluid flow in fractured porous media on Ω, which composes of matrix and fracture domains, Ω_m and Ω_f, respectively. Let $\Omega \subset \mathbb{R}^d$ be the domain of interest in d-dimensional space where $d = 1, 2$, or 3 bounded by boundary, $\partial\Omega$. $\partial\Omega$ can be decomposed to pressure and flux boundaries, $\partial\Omega_p$ and $\partial\Omega_q$, respectively. The time domain is denoted by $\mathbb{T} = (0, \tau]$, where $\tau > 0$ is the final time.

The illustration of the equi-dimensional model is shown in Fig. 3a. This model composes of two matrix subdomains, Ω_{mi} where $i = 1, 2$, and one fracture subdomain, Ω_f. Note that, for the sake of simplicity, this setup is used to illustrate the governing equation with only two matrix subdomains, but in a general case, the domain may compose of n_m subdomains, i.e. $i = 1, 2, \dots, n_m$. Moreover, the domain may contain up to n_f fractures, where n_m and n_f are number of matrix subdomain and fracture, respectively. For simplicity, in this section we will consider $n_f = 1$. The fractures may not cut through the matrix domain, which we call immersed fracture setting. This topic will be discussed in Section 3. The governing system with initial and boundary conditions of the equi-dimensional model assuming a slightly compressible fluid for the matrix domain is presented below:

$$c\phi_{mi}\frac{\partial}{\partial t}\left(p_{mi}\right) - \nabla\cdot\frac{\boldsymbol{k}_{mi}}{\mu}(\nabla p_{mi} - \rho\mathbf{g}) = g_{mi} \text{ in } \Omega_{mi}\times\mathbb{T}, \text{ for } i = 1, 2, \tag{1}$$

$$p_m = p_{mD} \text{ on } \partial\Omega_p \times \mathbb{T}, \tag{2}$$

$$-\frac{\boldsymbol{k}_{mi}}{\mu}(\nabla p_{mi} - \rho\mathbf{g})\cdot\boldsymbol{n} = q_{mN} \text{ on } \partial\Omega_q \times \mathbb{T}, \tag{3}$$

$$p_{mi} = p_{mi}^0 \text{ in } \Omega_{mi}\times\mathbb{T} \text{ at } t = 0, \text{ for } i = 1, 2, \tag{4}$$

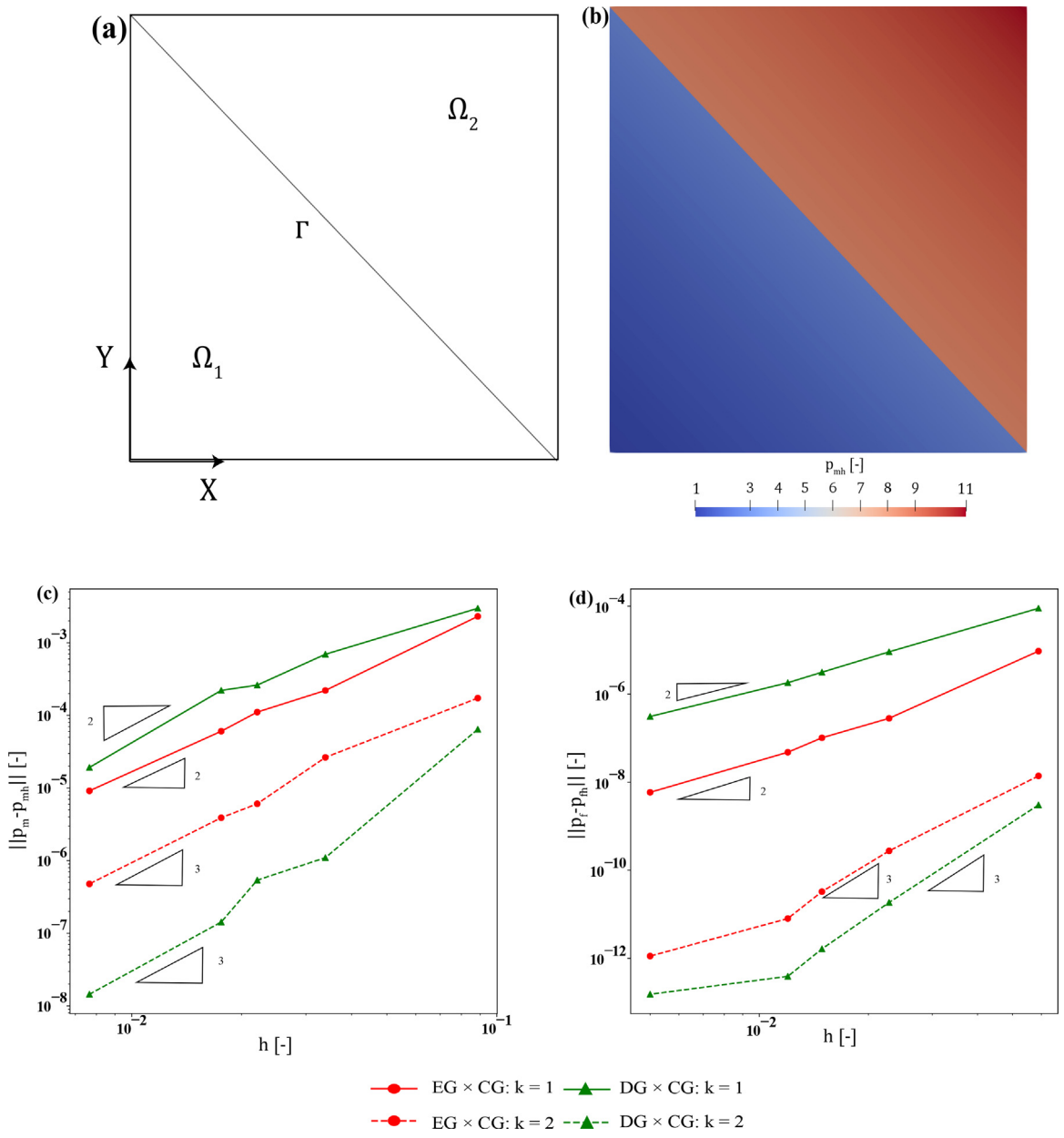

Fig. 5. (**a**) geometry used for the error convergence analysis, (**b**) illustration of the exact solution, error convergence plot between EG and DG methods with polynomial approximation degree 1 and 2 of (**c**) matrix and (**d**) fracture domains. Note that for (**c**) the slopes of the best fitted line are 2.235 (EG), 2.022 (DG) for the polynomial approximation degree 1, and 3.137 (EG), and 3.410 (DG) for the polynomial approximation degree 2. The slopes of the best fitted line for (**d**) are 2.289 (EG), 2.313 (DG) for the polynomial approximation degree 1, and 3.194 (EG), and 2.948 (DG) for the polynomial approximation degree 2.

and for the fracture domain is:

$$c\phi_f \frac{\partial}{\partial t}(p_f) - \nabla \cdot \frac{\boldsymbol{k}_f}{\mu}(\nabla p_f - \rho \mathbf{g}) = g_f \text{ in } \Omega_f \times \mathbb{T}, \tag{5}$$

$$p_f = p_{fD} \text{ on } \partial\Omega_p \times \mathbb{T}, \tag{6}$$

$$-\frac{\boldsymbol{k}_f}{\mu}(\nabla p_f - \rho \mathbf{g}) \cdot \boldsymbol{n} = q_{fN} \text{ on } \partial\Omega_q \times \mathbb{T}, \tag{7}$$

$$p_f = p_f^0 \text{ in } \Omega_f \times \mathbb{T} \text{ at } t = 0, \tag{8}$$

where $(\cdot)_i$ represents an index, c is the fluid compressibility, ϕ_m and ϕ_f are the matrix and fracture porosity (ϕ_f is assumed to be one), $\boldsymbol{k_m}$ and $\boldsymbol{k_f}$ are the matrix and fracture permeability tensor, respectively, μ is fluid viscosity, p_m and p_f are matrix and fracture pressure, respectively, ρ is fluid density, $\mathbf{g}$ is the gravitational vector, g_m and g_f are sink/source for matrix and fracture domains, respectively, $\boldsymbol{n}$ is a normal unit vector to any surfaces, p_{mD} and p_{fD} are prescribed pressure for matrix and fracture domains, respectively, q_{mN} and q_{fN} are prescribed flux for matrix and fracture domains, respectively, and $p_{m_i}^0$ and p_f^0 are prescribed pressure for matrix and fracture domains at $t = 0$, respectively.

To formulate the mixed-dimensional setting as presented in Fig. 3b, we integrate along the normal direction to the fracture plane Martin et al. (2005). As a result Ω_f is reduced to an interface, Γ. Note that the governing equation of the mixed-dimensional setting used in this study is proposed by Martin et al. (2005) in the mixed finite element formulation, which uses fluid pressure and fluid velocity as the primary variables. The mixed-dimensional setting has been used in the mixed formulation (Keilegavlen et al., 2017) or adapted to finite volume discretization (Glaser et al., 2017; Stefansson et al., 2018;

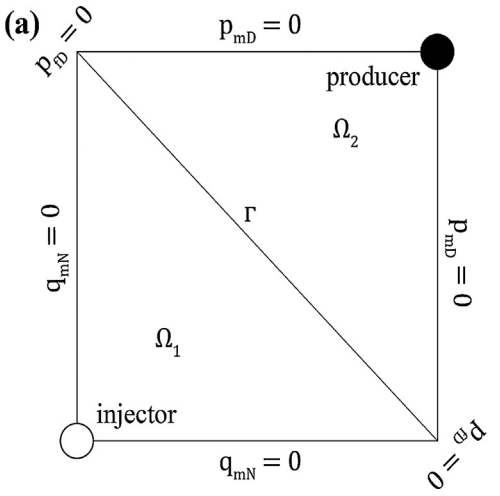

Fig. 6. (**a**) geometry and boundary conditions used for the quarter five-spot problem and (**b**) mesh that has $h = 1.2 \times 10^{-1}$.

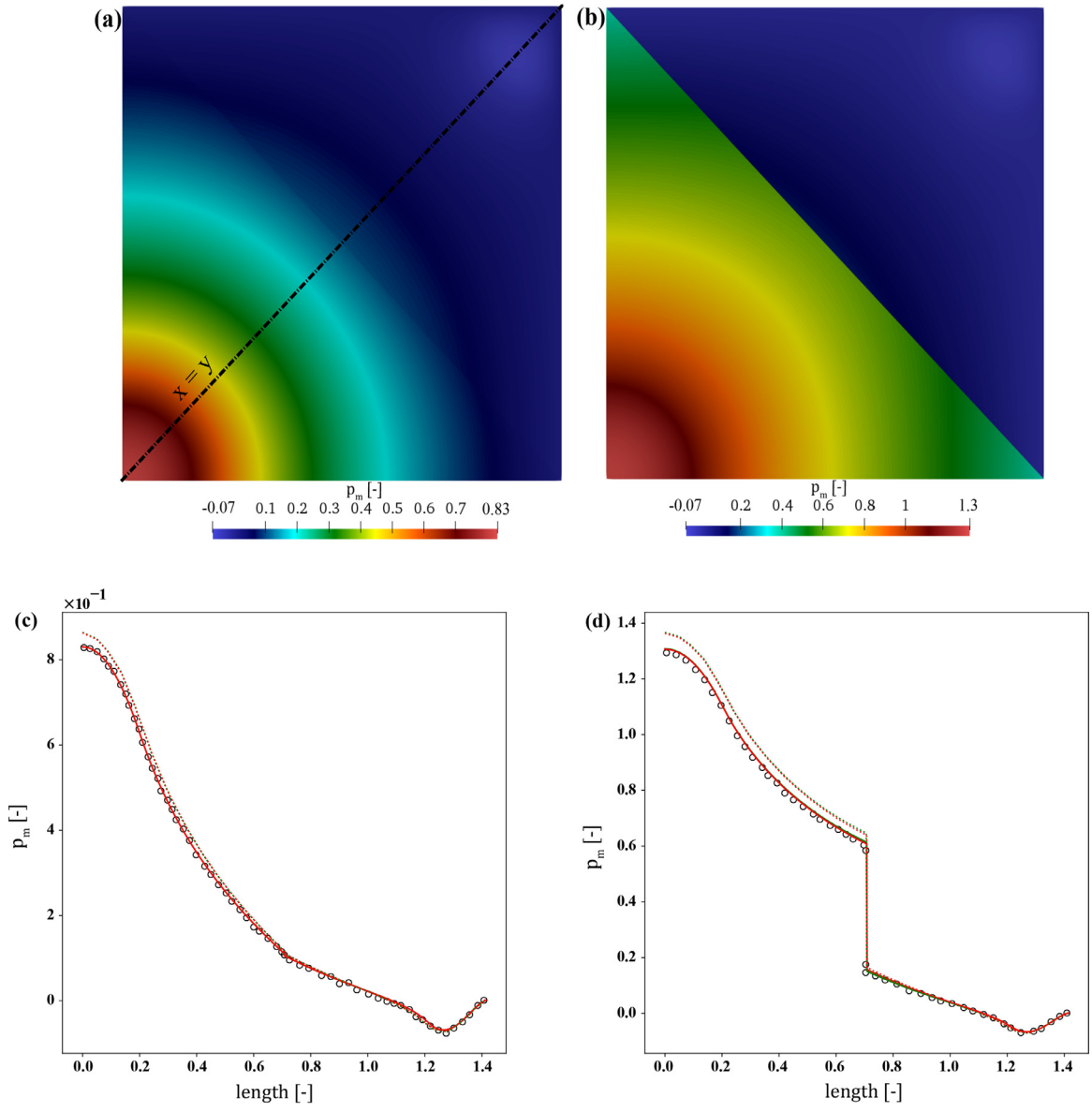

Fig. 7. Pressure solution with $h = 7.2 \times 10^{-2}$, p_m, in the matrix of quarter five-spot example: (**a**) permeable fracture, (**b**) impermeable fracture cases, p_m plot along $x = y$ line of (**c**) permeable fracture, and (**d**) impermeable fracture cases. Note that we digitize the results of the reference solution from Antonietti et al. (2019). Note that the results obtained with the EG and DG methods overlap.

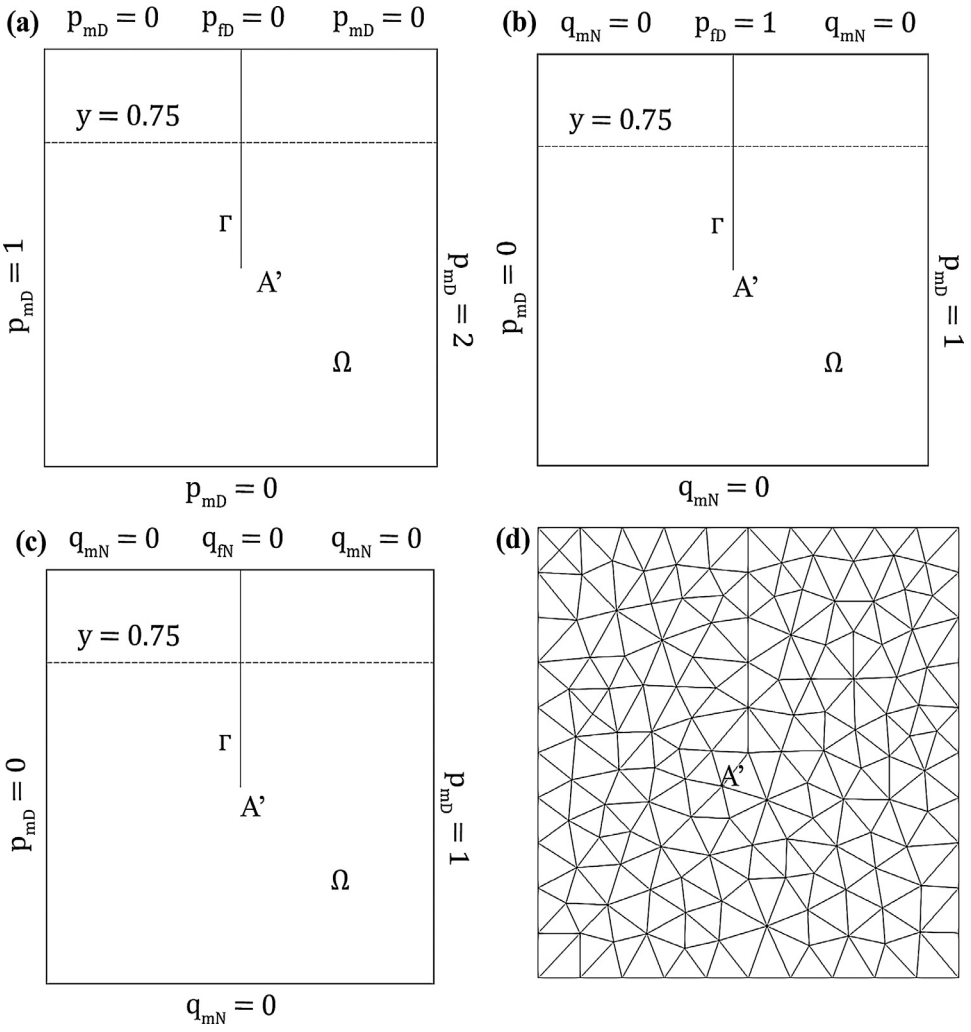

Fig. 8. Immersed fracture geometry and boundary conditions of (**a**) permeable fracture, (**b**) partially permeable fracture, (**c**) impermeable fracture cases, and (**d**) mesh that has $n_e = 272$. A' is fracture tip.

Glaser et al., 2019) and DG discretization on polytopic grids (Antonietti et al., 2019). The mixed-dimension strong formulation and its boundary conditions for the matrix domain are similar to the equi-dimensional model, (1) to (3), but the strong formulation and its boundary conditions of the fracture domain are:

$$ca_f \frac{\partial}{\partial t}(p_f) - \nabla^T \cdot a_f \frac{\boldsymbol{k}_f^T}{\mu}(\nabla^T p_f - \rho \mathbf{g}) = g_f + [\![-\frac{\boldsymbol{k_m}}{\mu}(\nabla p_m - \rho \mathbf{g})]\!] \text{ in } \Gamma \times \mathbb{T}, \tag{9}$$

$$p_f = p_{fD} \text{ on } \partial\Gamma_p \times \mathbb{T}, \tag{10}$$

$$-\frac{\boldsymbol{k}_f^T}{\mu}(\nabla p_f - \rho \mathbf{g}) \cdot \boldsymbol{n} = q_{fN} \text{ on } \partial\Gamma_q \times \mathbb{T}, \tag{11}$$

$$p_f = p_f^0 \text{ in } \Gamma \times \mathbb{T} \text{ at } t = 0, \tag{12}$$

where $\partial\Gamma_p$ and $\partial\Gamma_q$ represent pressure and flux boundaries of the fracture domain, respectively, $\boldsymbol{k}_f^T$ is the tangential fracture permeability tensor, ∇^T and $\nabla^T \cdot$ are the tangential gradient and divergence operators, which are defined as $\nabla^T(\cdot) = \nabla(\cdot) - \boldsymbol{n}[\boldsymbol{n} \cdot \nabla(\cdot)]$ and $\mathrm{tr}\left(\nabla^T(\cdot)\right)$, respectively, $\mathrm{tr}(\cdot)$ is trace operator, a_f is a fracture aperture, $[\![-\frac{\boldsymbol{k_m}}{\mu}(\nabla p_m - \rho \mathbf{g})]\!]$ represents the fluid mass transfer between matrix and fracture domains Martin et al. (2005), $[\![\cdot]\!]$ is jump operator, which will be discussed later in the discretization part, and p_{fD} and q_{fN} are specified pressure and flux for the fracture domain, respectively.

In this study, if $d = 3$, $\boldsymbol{k_m}$ as a full tensor is defined as:

$$\boldsymbol{k_m} := \begin{bmatrix} k_m^{xx} & k_m^{xy} & k_m^{xz} \\ k_m^{yx} & k_m^{yy} & k_m^{yz} \\ k_m^{zx} & k_m^{zy} & k_m^{zz} \end{bmatrix}, \tag{13}$$

where all tensor components characterize the transformation of the components of the gradient of fluid pressure into the components of the velocity vector. The k_m^{xx}, k_m^{yy}, and k_m^{zz} represent the matrix permeability in x-, y-, and z-direction, respectively. $\boldsymbol{k_f}$, on the other hand, composes of two components:

$$\boldsymbol{k}_f := \begin{bmatrix} \boldsymbol{k}_f^T & 0 \\ 0 & k_f^n \end{bmatrix}, \tag{14}$$

where k_f^n is the normal fracture permeability. Note that we present here a general form of $\boldsymbol{k}_f^T$, to be specific, $\boldsymbol{k}_f^T$ is a scalar if $d = 2$ and tensor if $d = 3$. To represent the fluid mass transfer between matrix and fracture domains, following Martin et al. (2005), Antonietti et al. (2019), we define the coupling conditions between the matrix and fracture domain as:

$$\langle -\frac{\boldsymbol{k_m}}{\mu}(\nabla p_m - \rho \mathbf{g}) \rangle \cdot \boldsymbol{n} = \frac{\alpha_f}{2}\left(p_{m_1} - p_{m_2}\right) \text{ on } \Gamma, \tag{15}$$

$$[\![-\frac{\boldsymbol{k_m}}{\mu}(\nabla p_m - \rho \mathbf{g})]\!] = \frac{2\alpha_f}{2\xi - 1}\left(\langle p_m \rangle - p_f\right) \text{ on } \Gamma, \tag{16}$$

where $\langle \cdot \rangle$ is an average operator, which will be presented later in the discretization part, α_f represents a resistant factor of the mass transfer

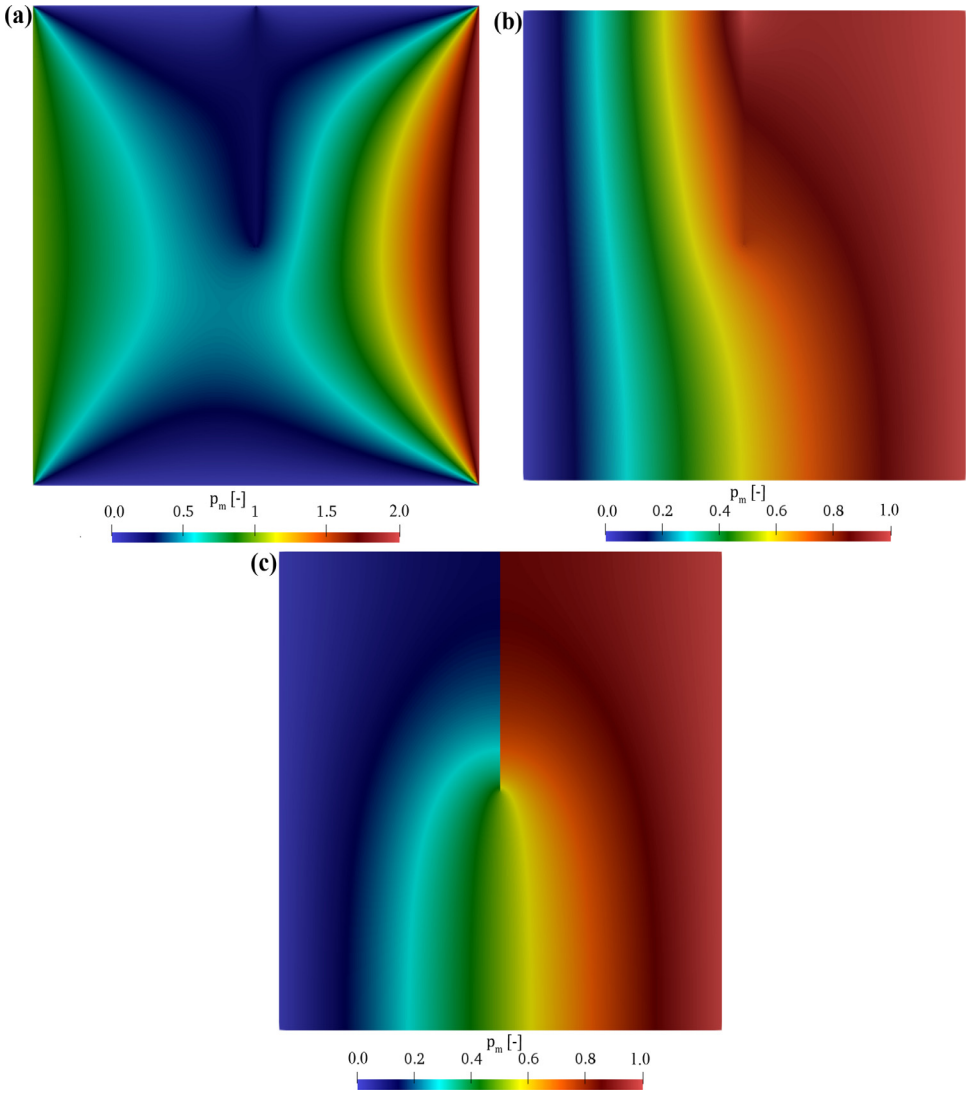

Fig. 9. Pressure solution, p_m, in the matrix of immersed fracture example using $n_e = 6,698$: (**a**) permeable fracture, (**b**) partially permeable fracture, and (**c**) impermeable fracture cases.

between the fracture and matrix domains defined as:

$$\alpha_f = \frac{2k_f^n}{a_f}, \tag{17}$$

and $\xi \in (0.5, 1.0]$. In this paper, we set $\xi = 1.0$ for the sake of simplicity. In general case, ξ is used to represent a family of the mixed-dimensional model, and more details can be found in Martin et al. (2005), Antonietti et al. (2019).

2.2. Numerical discretization

In this section, the discretization of the mixed-dimensional model is illustrated. The domain Ω is partitioned into n_e elements, $\mathcal{T}_h$, which is the family of elements T (triangles in 2D, tetrahedrons in 3D). We will further denote by e a face of T as illustrated in Fig. 4. We denote h_T as the diameter of T and define $h := \max(h_T)$, which we may refer as mesh size. Let $\mathcal{E}_h$ denotes the set of all facets, for the matrix domain, $\mathcal{E}_h^0$ the internal facets, $\mathcal{E}_h^D$ the Dirichlet boundary faces, and $\mathcal{E}_h^N$ denotes the Neumann boundary faces. Following Lee et al. (2016a) for any $e \in \mathcal{E}_h^0$ let T^+ and T^- be two neighboring elements such that $e = \partial T^+ \cap \partial T^-$. Let $\boldsymbol{n}^+$ and $\boldsymbol{n}^-$ be the outward normal unit vectors to ∂T^+ and ∂T^-, respectively (see Fig. 4a). $\mathcal{E}_h = \mathcal{E}_h^0 \cup \mathcal{E}_h^D \cup \mathcal{E}_h^N$, $\mathcal{E}_h^0 \cap \mathcal{E}_h^D = \emptyset$, $\mathcal{E}_h^0 \cap \mathcal{E}_h^N = \emptyset$, and $\mathcal{E}_h^D \cap \mathcal{E}_h^N = \emptyset$. We further define $\mathcal{E}_h^1 := \mathcal{E}_h^0 \cup \mathcal{E}_h^D$.

The fracture domain is conforming with $\mathcal{E}_h$, and it is named Γ_h (intervals in 2D, triangles in 3D domain) hereafter as presented in Fig. 4b. We will further denote by e_f a face of Γ_h. Let Λ_h denotes the set of all facets, for the fracture domain, Λ_h^0 the internal facets, Λ_h^D the Dirichlet boundary faces, and Λ_h^N denotes the Neumann boundary faces, and $\Lambda_h^D \cap \Lambda_h^N = \emptyset$. Let $\boldsymbol{n}$ be the outward normal unit vector to Γ_h, which is coincided with $\boldsymbol{n}^+$ of the ∂T^+.

Next, we define the jump operator of the scalar and vector values as:

$$\begin{aligned} [\![X \cdot \boldsymbol{n}]\!] &:= X^+\boldsymbol{n}^+ + X^-\boldsymbol{n}^- \text{ and} \\ [\![\boldsymbol{X} \cdot \boldsymbol{n}]\!] &:= \boldsymbol{X}^+ \cdot \boldsymbol{n}^+ + \boldsymbol{X}^- \cdot \boldsymbol{n}^-, \end{aligned} \tag{18}$$

respectively, Moreover, by assuming that the normal vector n is oriented from T^+ to T^-, we obtain

$$[\![X]\!] := X^+ - X^- \tag{19}$$

Following Lee et al. (2016a), Scovazzi et al. (2017), the weighted average is defined as:

$$\langle X \rangle_{\delta e} = \delta_e X^+ + (1 - \delta_e) X^-, \tag{20}$$

where

$$\delta_e := \frac{k_{m_e}^-}{k_{m_e}^+ + k_{m_e}^-}, \tag{21}$$

and

$$k_{m_e}^+ := (\boldsymbol{n}^+)^T \cdot \boldsymbol{k_m}^+ \cdot \boldsymbol{n}^+,$$

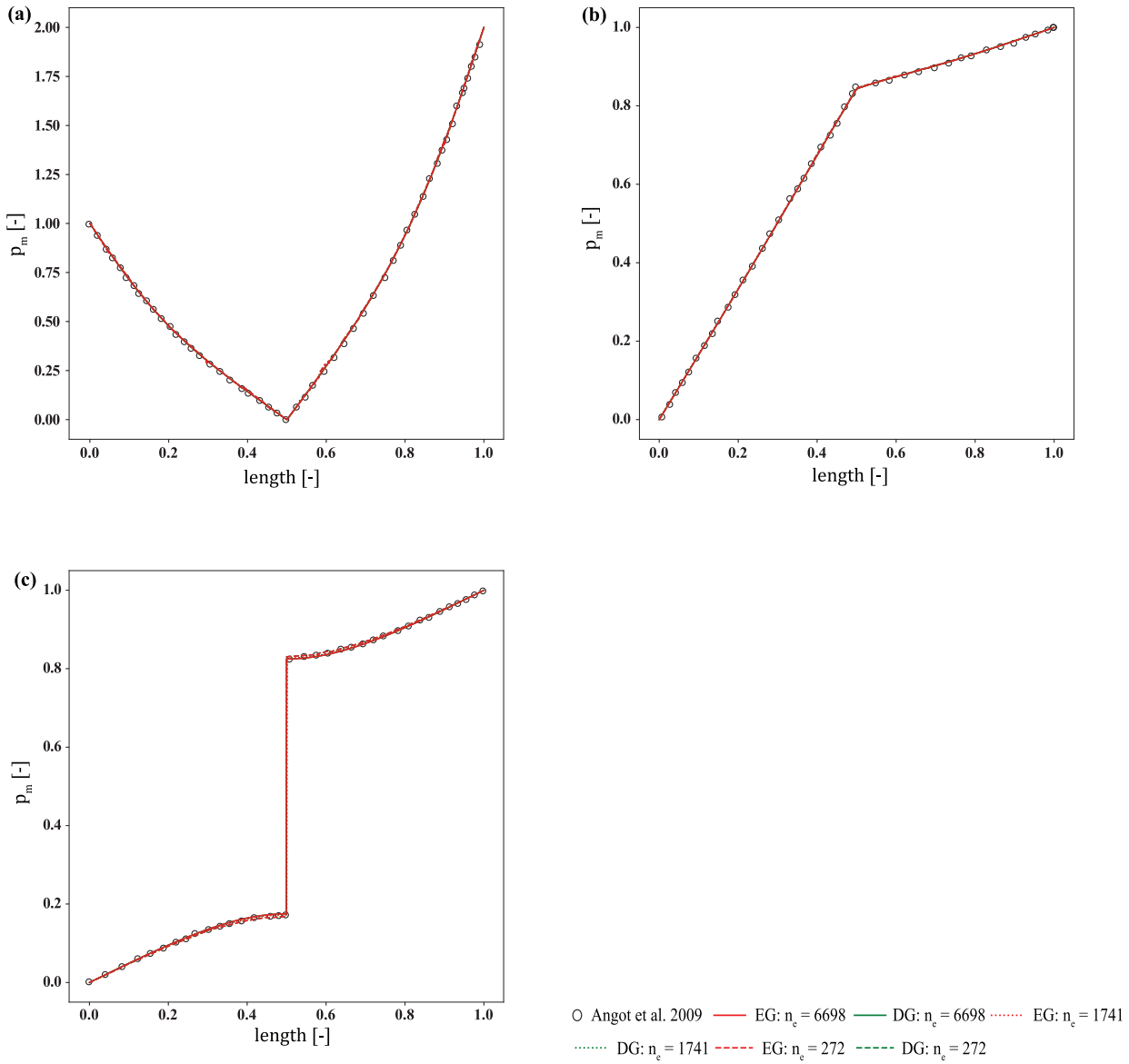

Fig. 10. p_m plot along $y = 0.75$ line of immersed fracture example: (**a**) permeable fracture, (**b**) partially permeable fracture, (**c**) impermeable fracture cases. Note that we digitize the reference results, Angot et al. 2009, from Angot et al. (2009). All the results obtained from the EG and DG methods with different mesh sizes overlap.

$$k_{m_e}^{-} := (\boldsymbol{n}^{-})^T \cdot \boldsymbol{k_m}^{-} \cdot \boldsymbol{n}^{-}, \tag{22}$$

and a harmonic average of $k_{m_e}^{+}$ and $k_{m_e}^{-}$ is defined as:

$$k_{m_e} := \frac{2k_{m_e}^{+}k_{m_e}^{-}}{\left(k_{m_e}^{+} + k_{m_e}^{-}\right)}. \tag{23}$$

The arithmetic average, $\delta_e = 0.5$, is simply denoted by $\langle \cdot \rangle$. Note that, in general case, δ_e is also defined for the $\boldsymbol{k_f}$; however, for the sake of simplicity, we assume the material properties of the fracture domain are homogeneous. Hence, we perform these operators in the matrix domain only.

Remark 1. The numerical discretization discussed in this study only considers the case of a conforming mesh, i.e. the fracture domain, Γ, element is coincident with a set of faces of the matrix domain, Ω, as illustrated in Fig. 4b.

This study focuses on two function spaces, arising from EG, and DG discretizations, respectively. We begin with defining the CG function space for the matrix pressure, p_m as

$$\mathcal{P}_h^{\mathrm{CG}_k}(\mathcal{T}_h) := \left\{\psi_m \in \mathbb{C}^0(\Omega) : \psi_m|_T \in \mathbb{P}_k(T), \forall T \in \mathcal{T}_h\right\}, \tag{24}$$

where $\mathcal{P}_h^{\mathrm{CG}_k}(\mathcal{T}_h)$ is the space for the CG approximation with kth degree polynomials for the p_m unknown, $\mathbb{C}^0(\Omega)$ denotes the space of scalar-valued piecewise continuous polynomials, $\mathbb{P}_k(T)$ is the space of polynomials of degree at most k over each element T, and ψ_m denotes a generic function of $\mathcal{P}_h^{\mathrm{CG}_k}(\mathcal{T}_h)$. Furthermore, we define the following DG function space for the matrix pressure, p_m:

$$\mathcal{P}_h^{\mathrm{DG}_k}(\mathcal{T}_h) := \left\{\psi_m \in L^2(\Omega) : \psi_m|_T \in \mathbb{P}_k(T), \forall T \in \mathcal{T}_h\right\}, \tag{25}$$

where $\mathcal{P}_h^{\mathrm{DG}_k}(\mathcal{T}_h)$ is the space for the DG approximation with kth degree polynomials for the p_m space and $L^2(\Omega)$ is the space of square integrable functions. Finally, we define the EG function space for p_m as:

$$\mathcal{P}_h^{\mathrm{EG}_k}(\mathcal{T}_h) := \mathcal{P}_h^{\mathrm{CG}_k}(\mathcal{T}_h) + \mathcal{P}_h^{\mathrm{DG}_0}(\mathcal{T}_h), \tag{26}$$

where $\mathcal{P}_h^{\mathrm{EG}_k}(\mathcal{T}_h)$ is the space for the EG approximation with kth degree polynomials for the p space and $\mathcal{P}_h^{\mathrm{DG}_0}(\mathcal{T}_h)$ is the space for the DG approx-

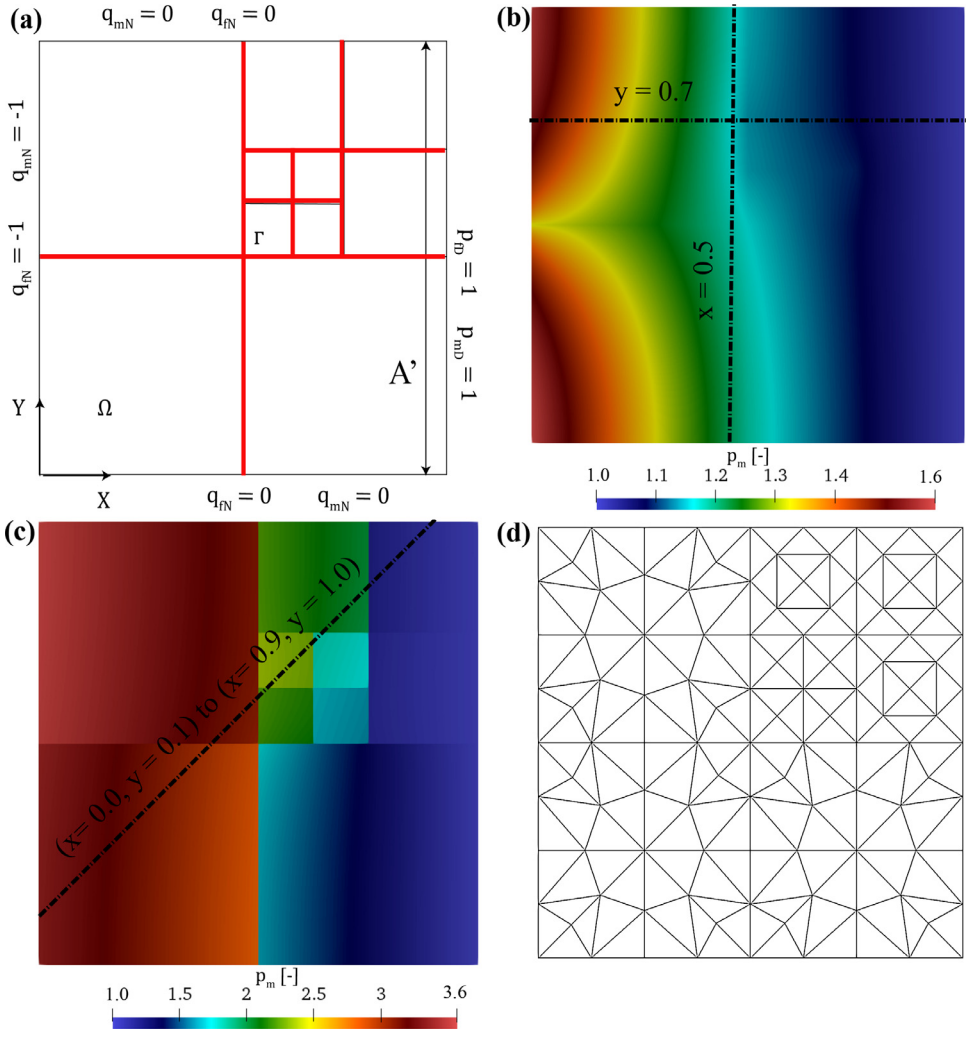

Fig. 11. Regular fracture network example: (**a**) geometry and boundary conditions (fractures are shown in red), pressure solution, p_m, in the matrix using $n_e = 2046$ of (**b**) permeable fracture, (**c**) impermeable fracture cases, and (**d**) mesh that has $n_e = 184$. (For interpretation of the references to colour in this figure legend, the reader is referred to the web version of this article.)

imation with 0th degree polynomials, in other words, a piecewise constant approximation. Note that the EG discretization is expected to be beneficial for an accurate approximation of the p_m discontinuity across interfaces where high permeability contrast, either between $\boldsymbol{k}_{\boldsymbol{m}}^{+}$ and $\boldsymbol{k}_{\boldsymbol{m}}^{-}$ or $\boldsymbol{k}_{\boldsymbol{m}}$ and $\boldsymbol{k}_{\boldsymbol{f}}$, is observed. On the other hand, the material properties of the fracture domain are assumed to be homogeneous, which leads to no discontinuity within the fracture domain. Therefore, the CG discretization of the p_f unknown will suffice in the following. The p_f function space is defined as:

$$\mathcal{P}_h^{\mathrm{CG}_k}(\Gamma_h) := \left\{ \psi_f \in \mathbb{C}^0(\Gamma) : \psi_f\big|_e \in \mathbb{P}_k(e), \forall e \in \Gamma_h \right\}, \tag{27}$$

where $\mathcal{P}_h^{\mathrm{CG}_k}(\Gamma_h)$ is the space for the CG approximation with kth degree polynomials for the p_f unknown, $\mathbb{C}^0(\Gamma)$ denotes the space of scalar-valued piecewise continuous polynomials, $\mathbb{P}_k(e)$ is the space of polynomials of degree at most k over each facet e, and ψ_f denotes a generic function of $\mathcal{P}_h^{\mathrm{CG}_k}(\Gamma_h)$.

Remark 2. In this study, we only focus on the mixed function space between the matrix and fracture domains arising from either $\mathcal{P}_h^{\mathrm{EG}_k}(\mathcal{T}_h) \times \mathcal{P}_h^{\mathrm{CG}_k}(\Gamma_h)$ or $\mathcal{P}_h^{\mathrm{DG}_k}(\mathcal{T}_h) \times \mathcal{P}_h^{\mathrm{CG}_k}(\Gamma_h)$. The fracture domain can be discretized by either $\mathcal{P}_h^{\mathrm{EG}_k}(\Gamma_h)$ or $\mathcal{P}_h^{\mathrm{DG}_k}(\Gamma_h)$ if there are any discontinuities inside the fracture medium.

The time domain, $\mathbb{T} = (0, \tau]$, is partitioned into N_t open subintervals such that, $0 =: t^0 < t^1 < \cdots < t^{N_t} := \tau$. The length of the subinterval, Δt^n, is defined as $\Delta t^n = t^n - t^{n-1}$ where n represents the current time step. In this study, implicit first-order time discretization is utilized for a time domain of (1) and (5) as shown below for both $p_{m,h}^n$ and $p_{f,h}^n$:

$$\frac{\partial p_{m,h}}{\partial t} \approx \frac{p_{m,h}^n - p_{m,h}^{n-1}}{\Delta t^n}, \text{ and } \frac{\partial p_{f,h}}{\partial t} \approx \frac{p_{f,h}^n - p_{f,h}^{n-1}}{\Delta t^n}. \tag{28}$$

We denote that the temporal approximation of the function $\Phi(\cdot, t^n)$ by Φ^n.

With given $p_{m,h}^{n-1}$ and $p_{f,h}^{n-1}$, we now seek the approximated solutions $p_{m,h}^n \in \mathcal{P}_h^{\mathrm{EG}_k}(\mathcal{T}_h)$ and $p_{f,h}^n \in \mathcal{P}_h^{\mathrm{CG}_k}(\Gamma_h)$ of $p_m(\cdot, t^n)$ and $p_f(\cdot, t^n)$, respectively, satisfying

$$\begin{aligned} &\mathcal{M}\Big(\big(p_{m,h}^n, p_{f,h}^n; p_{m,h}^{n-1}, p_{f,h}^{n-1}\big), (\psi_m, \psi_f)\Big) \\ &\quad + \mathcal{A}\Big(\big(p_{m,h}^n, p_{f,h}^n\big), (\psi_m, \psi_f)\Big) - \mathcal{L}(\psi_m, \psi_f) = 0, \\ &\quad \forall \psi_m \in \mathcal{P}_h^{\mathrm{EG}_k}(\mathcal{T}_h) \text{ and } \forall \psi_f \in \mathcal{P}_h^{\mathrm{CG}_k}(\Gamma_h). \end{aligned} \tag{29}$$

First, the temporal discretization part is defined as

$$\begin{aligned} \mathcal{M}\Big(\big(p_{m,h}^n, p_{f,h}^n; p_{m,h}^{n-1}, p_{f,h}^{n-1}\big), (\psi_m, \psi_f)\Big) &:= m_m\Big(p_{m,h}^n; p_{m,h}^{n-1}, \psi_m\Big) \\ &+ m_f\Big(p_{f,h}^n; p_{f,h}^{n-1}, \psi_f\Big), \end{aligned} \tag{30}$$

where

$$m_m\Big(p_{m,h}^n; p_{m,h}^{n-1}, \psi_m\Big) := \sum_{T \in \mathcal{T}_h} \int_T c\phi_m \frac{p_{m,h}^n - p_{m,h}^{n-1}}{\Delta t^n} \psi_m \, dV, \tag{31}$$

and

$$m_f\Big(p_{f,h}^n; p_{f,h}^{n-1}, \psi_f\Big) := \sum_{e \in \Gamma_h} \int_e c a_f \frac{p_{f,h}^n - p_{f,h}^{n-1}}{\Delta t^n} \psi_f \, dS. \tag{32}$$

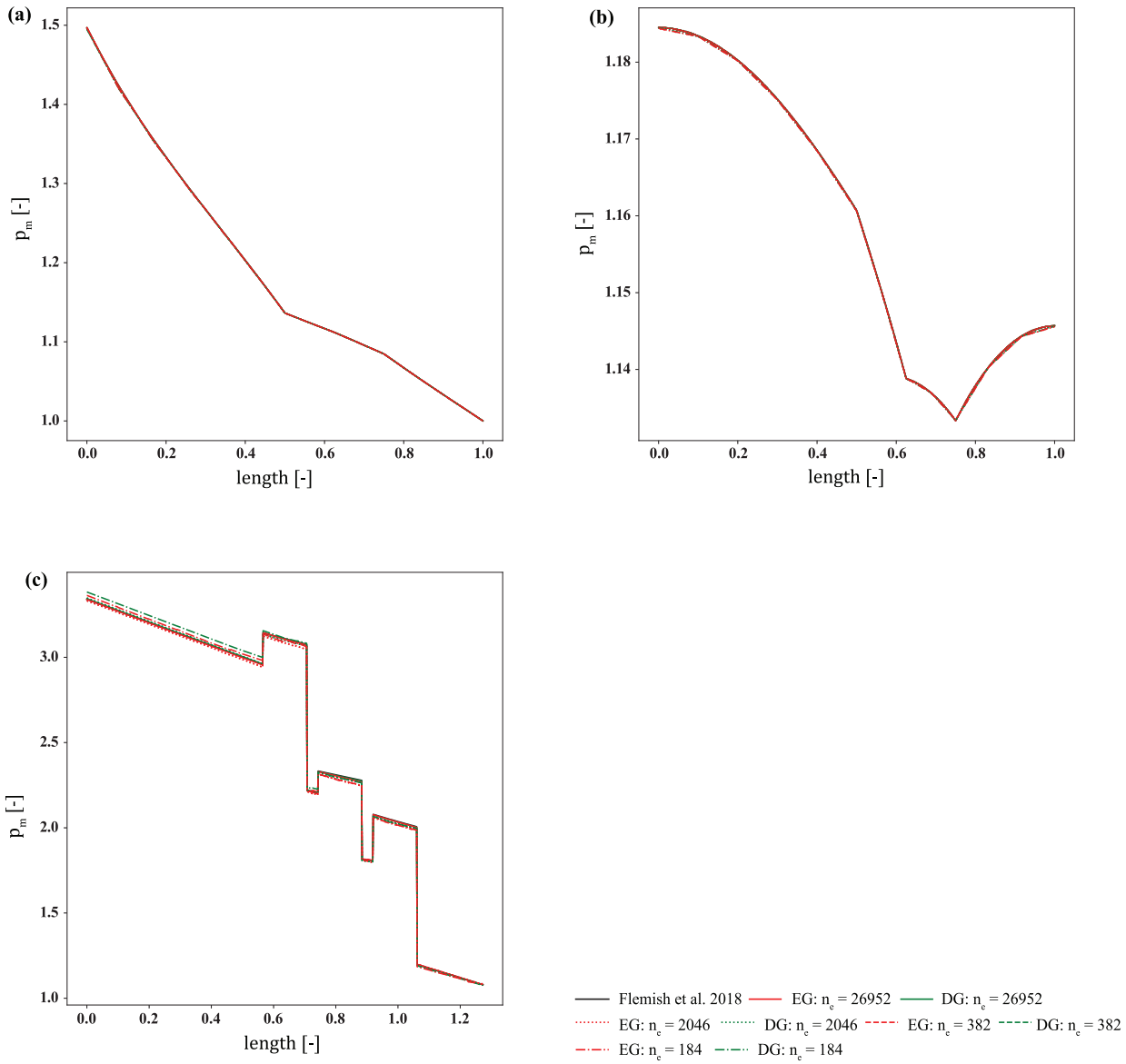

Fig. 12. p_m plot of regular fracture network example: (**a**) along $y = 0.7$ line of permeable fracture, (**b**) along $x = 0.5$ line of permeable fracture, (**c**) along $(x = 0.0, y = 0.1)$ to $(x = 0.9, y = 1.0)$ line of impermeable fracture cases. All of the results obtained from the EG and DG methods of permeable fractures with different mesh sizes overlap. The results of impermeable fractures case with different mesh sizes, however, illustrate some differences.

Here, $\int_T \cdot \, dV$ and $\int_e \cdot \, dS$ refer to volume and surface integrals, respectively.

Next, we define $\mathcal{A}\left(\left(p^n_{m,h}, p^n_{f,h}\right), \left(\psi_m, \psi_f\right)\right)$ as:

$$\begin{aligned}\mathcal{A}\left(\left(p^n_{m,h}, p^n_{f,h}\right), \left(\psi_m, \psi_f\right)\right) &:= a\left(p^n_{m,h}, \psi_m\right) + b\left(p^n_{f,h}, \psi_m\right) \\ &+ c\left(p^n_{m,h}, \psi_f\right) + d\left(p^n_{f,h}, \psi_f\right),\end{aligned} \tag{33}$$

where

$$\begin{aligned}a\left(p^n_{m,h}, \psi_m\right) :=& \sum_{T\in\mathcal{T}_h} \int_T \frac{\boldsymbol{k_m}}{\mu}\left(\nabla p^n_{m,h} - \rho\mathbf{g}\right)\cdot\nabla\psi_m \, dV \\ &- \sum_{e\in\mathcal{E}^1_h\setminus\Gamma_h} \int_e \langle \frac{\boldsymbol{k_m}}{\mu}\left(\nabla p^n_{m,h} - \rho\mathbf{g}\right)\rangle_{\delta_e}\cdot[\![\psi_m]\!]\, dS \\ &+ \theta \sum_{e\in\mathcal{E}^1_h\setminus\Gamma_h} \int_e \langle \frac{\boldsymbol{k_m}}{\mu}\nabla\psi_m\rangle_{\delta_e}\cdot[\![p^n_{m,h}]\!]\, dS \\ &+ \sum_{e\in\mathcal{E}^1_h\setminus\Gamma_h} \int_e \frac{\beta}{h_e}\frac{k_{me}}{\mu}[\![p^n_{m,h}]\!]\cdot[\![\psi_m]\!]\, dS \\ &+ \sum_{e\in\Gamma_h} \int_e \frac{\alpha_f}{2}[\![p^n_{m,h}]\!]\cdot[\![\psi_m]\!]\, dS \\ &+ \sum_{e\in\Gamma_h} \int_e \frac{2\alpha_f}{2\xi-1}\langle p^n_{m,h}\rangle\langle\psi_m\rangle\, dS,\end{aligned} \tag{34}$$

$$b\left(p^n_{f,h}, \psi_m\right) := -\sum_{e\in\Gamma_h} \int_e \frac{2\alpha_f}{2\xi-1} p^n_{f,h}\langle\psi_m\rangle\, dS, \tag{35}$$

$$c\left(p^n_{m,h}, \psi_f\right) := -\sum_{e\in\Gamma_h} \int_e \frac{2\alpha_f}{2\xi-1}\langle p^n_{m,h}\rangle\psi_f\, dS, \tag{36}$$

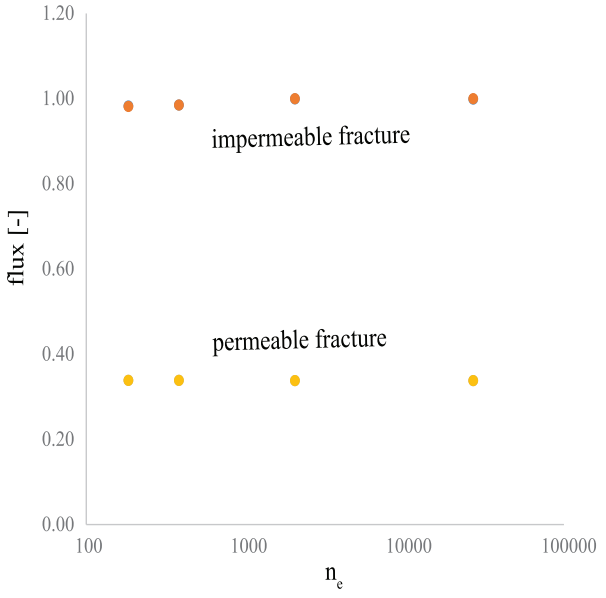

Fig. 13. flux at surface A' comparison for both permeable and impermeable cases between the EG and DG methods. All of the results obtained from the EG and DG methods with different mesh sizes overlap.

and

$$d\left(p^n_{f,h},\psi_f\right) := \sum_{e\in\Gamma_h}\int_e a_f \frac{\boldsymbol{k}^{\boldsymbol{T}}_{\boldsymbol{f}}}{\mu}\left(\nabla p^n_{f,h} - \rho\mathbf{g}\right)\cdot\nabla\psi_f\, dS + \sum_{e\in\Gamma_h}\int_e \frac{2\alpha_f}{2\xi-1}p^n_{f,h}\psi_f\, dS, \tag{37}$$

We note that the coupling conditions, (15) and (16), are embedded in the above discretized equations. In particular, the conditions (15) and (16) are discretized as

$$\mathcal{I}_1\left(p^n_{m,h},\psi_m\right) := \sum_{e\in\Gamma_h}\int_e \frac{\alpha_f}{2}[\![p^n_{m,h}]\!]\cdot[\![\psi_m]\!]\, dS, \quad \forall\psi_m\in\mathcal{P}_h^{\mathrm{EG}_k}(\mathcal{T}_h), \tag{38}$$

and

$$\mathcal{I}_2\left(\left(p^n_{m,h},p^n_{f,h}\right),\left(\psi_m,\psi_f\right)\right) := \sum_{e\in\Gamma_h}\int_e \frac{2\alpha_f}{2\xi-1}\langle p^n_{m,h}\rangle\langle\psi_m\rangle\, dS - \sum_{e\in\Gamma_h}\int_e \frac{2\alpha_f}{2\xi-1}\langle p^n_{m,h}\rangle\psi_f\, dS - \sum_{e\in\Gamma_h}\int_e \frac{2\alpha_f}{2\xi-1}p^n_{f,h}\langle\psi_m\rangle\, dS + \sum_{e\in\Gamma_h}\int_e \frac{2\alpha_f}{2\xi-1}p^n_{f,h}\psi_f\, dS, \quad \forall\psi_m\in\mathcal{P}_h^{\mathrm{EG}_k}(\mathcal{T}_h) \text{ and } \forall\psi_f\in\mathcal{P}_h^{\mathrm{CG}_k}(\Gamma_h), \tag{39}$$

respectively. Finally, we define $\mathcal{L}(\psi_m,\psi_f)$ as:

$$\mathcal{L}\left(\psi_m,\psi_f\right) := \ell_m(\psi_m) + \ell_f(\psi_f) \tag{40}$$

where

$$\ell_m(\psi_m) := \sum_{T\in\mathcal{T}_h}\int_T g_m\psi_m\, dV + \sum_{e\in\mathcal{E}_h^N}\int_e q_{mN}\psi_m\, dS + \theta\sum_{e\in\mathcal{E}_h^D}\int_e \frac{\boldsymbol{k_m}}{\mu}\nabla\psi_m\cdot p_{mD}\boldsymbol{n}\, dS + \sum_{e\in\mathcal{E}_h^D}\int_e \frac{\beta}{h_e}\frac{k_{me}}{\mu}[\![\psi_p]\!]\cdot p_{mD}\boldsymbol{n}\, dS \tag{41}$$

and

$$\ell_f(\psi_f) := \textstyle\sum_{e\in\Gamma_h}\int_e a_f g_f\psi_f\, dS + \sum_{e_f\in\Lambda_h^N}\int_e q_{fN}\psi_f\, dS. \tag{42}$$

Here, the choices of the interior penalty method is provided by θ. The discretization becomes the symmetric interior penalty Galerkin method (SIPG), when $\theta=-1$, the incomplete interior penalty Galerkin method (IIPG), when $\theta=0$, and the non-symmetric interior penalty Galerkin method (NIPG) when $\theta=1$ Riviere (2008). In this study, we set $\theta=-1$ for the simplicity. The interior penalty parameter, β, is a function of the polynomial degree, k, and the characteristic mesh size, h_e, which is defined as:

$$h_e := \frac{\mathrm{meas}\left(T^+\right)+\mathrm{meas}\left(T^-\right)}{2\,\mathrm{meas}(e)}, \tag{43}$$

where meas(·) represents a measurement operator, measuring length, area, or volume. Some studies for the optimal choice of β is provided in Lee et al. (2019), Riviere (2008).

Remark 3. The Neumann boundary condition is naturally applied on the boundary faces that belong to the Neumann boundary domain for both the matrix and fracture domains, $e\in\mathcal{E}_h^N$ and $e_f\in\Lambda_h^N$. The Dirichlet boundary condition, on the other hand, is weakly enforced on the Dirichlet boundary faces, $e\in\mathcal{E}_h^D$, for the matrix domain, but strongly enforced on the Dirichlet bondary faces of the fracture domain, $e_f\in\Lambda_h^D$.

Let $\{\psi_{m,\pi}{}^{(i_1)}\}_{i_1=1}^{\mathcal{N}_{p_{m,\pi}}}$ denote the set of basis functions of $\mathcal{P}_h^{\pi_k}(\mathcal{T}_h)$, i.e. $\mathcal{P}_h^{\pi_k}(\mathcal{T}_h)=\mathrm{span}\,\{\psi_m{}^{(i_1)}\}_{i_1=1}^{\mathcal{N}_{p_{m,\pi}}}$, having denoted by $\mathcal{N}_{p_{m,\pi}}$ the number of DOF for the π scalar-valued space, where π can mean either EG or DG. In a similar way, let $\{\psi_{f,\mathrm{CG}}^{(i_3)}\}_{i_3=1}^{\mathcal{N}_{p_f,\mathrm{CG}}}$ be the set of basis functions for the space $\mathcal{P}_h^{\mathrm{CG}_k}(\Gamma_h)$. $\mathcal{N}_{p_f,\mathrm{CG}}$ the number of DOF for the CG scalar-valued space. Hence, two mixed function spaces, ***(1)*** $\mathrm{EG}_k\times\mathrm{CG}_k$ and ***(2)*** $\mathrm{DG}_k\times\mathrm{CG}_k$ where k represents the degree of polynomial approximation, are possible, and will be compared in the numerical examples in the next section. The matrix corresponding to the left-hand side of (29) is assembled composing the following blocks:

$$\begin{aligned}
&\left[\mathcal{J}_{mm}^{\pi_k\times\pi_k}\right]_{i_1i_2} := m_m\left(\psi_m{}^{(i_2)},\psi_m{}^{(i_1)}\right)+a\left(\psi_m{}^{(i_2)},\psi_m{}^{(i_1)}\right),\ i_1 = 1,\dots,\mathcal{N}_{p_{m,\pi}}, i_2=1,\dots,\mathcal{N}_{p_{m,\pi}},\\
&\left[\mathcal{J}_{mf}^{\pi_k\times\mathrm{CG}_k}\right]_{i_ii_3} := b\left(\psi_{f,\mathrm{CG}}^{(i_3)},\psi_{m,\pi}{}^{(i_1)}\right),\ i_1=1,\dots,\mathcal{N}_{p_{m,\pi}}, i_3=1,\dots,\mathcal{N}_{p_{f,\mathrm{CG}}},\\
&\left[\mathcal{J}_{fm}^{\mathrm{CG}_k\times\pi_k}\right]_{i_4i_2} := c\left(\psi_{m,\pi}{}^{(i_2)},\psi_{p_f,\mathrm{CG}}^{(i_4)}\right),\ i_4=1,\dots,\mathcal{N}_{p_f,\mathrm{CG}}, i_2=1,\dots,\mathcal{N}_{p_{m,\pi}},\\
&\left[\mathcal{J}_{ff}^{\mathrm{CG}_k\times\mathrm{CG}_k}\right]_{i_4i_3} := m_f\left(\psi_{f,\mathrm{CG}}^{(i_3)},\psi_{f,\mathrm{CG}}^{(i_4)}\right)+d\left(\psi_{f,\mathrm{CG}}^{(i_3)},\psi_{f,\mathrm{CG}}^{(i_4)}\right) i_4 = 1,\dots,\mathcal{N}_{p_f,\mathrm{CG}}, i_3=1,\dots,\mathcal{N}_{p_f,\mathrm{CG}}.
\end{aligned} \tag{44}$$

In a similar way, the right-hand side of (29) gives rise to a block vector of components

$$\begin{aligned}
&\left[\ell_m^{\pi_k}\right]_{i_1} := \ell_m\left(\psi_{m,\pi}{}^{(i_1)}\right),\ i_1=1,\dots,\mathcal{N}_{p_{m,\pi}},\\
&\left[\ell_f^{\mathrm{CG}_k}\right]_{i_3} := \ell_f\left(\psi_{f,\mathrm{CG}}^{(i_3)}\right)\ i_3=1,\dots,\mathcal{N}_{f,\mathrm{CG}}.
\end{aligned} \tag{45}$$

The resulting block structure is thus

$$\begin{bmatrix}\mathcal{J}_{mm}^{\pi_k\times\pi_k} & \mathcal{J}_{mf}^{\pi_k\times\mathrm{CG}_k}\\ \mathcal{J}_{fm}^{\mathrm{CG}_k\times\pi_k} & \mathcal{J}_{ff}^{\mathrm{CG}_k\times\mathrm{CG}_k}\end{bmatrix}\begin{Bmatrix}p_{m,h}^{\pi_k}\\ p_{f,h}^{\mathrm{CG}_k}\end{Bmatrix} = \begin{Bmatrix}\ell_m^{\pi_k}\\ \ell_f^{\mathrm{CG}_k}\end{Bmatrix}. \tag{46}$$

where $p_{m,h}^{\pi_k}$ and $p_{f,h}^{\mathrm{CG}_k}$ collect the degrees of freedom for matrix and fracture pressure, respectively. Finally, we remark that (owing to (26)) the case $\pi=\mathrm{EG}$ can be equivalently decomposed into a $(\mathrm{CG}_k\times\mathrm{DG}_0)\times\mathrm{CG}_k$ mixed function space, resulting in:

$$\begin{bmatrix}\mathcal{J}_{mm}^{\mathrm{CG}_k\times\mathrm{CG}_k} & \mathcal{J}_{mm}^{\mathrm{CG}_k\times\mathrm{DG}_0} & \mathcal{J}_{mf}^{\mathrm{CG}_k\times\mathrm{CG}_k}\\ \mathcal{J}_{mm}^{\mathrm{DG}_0\times\mathrm{CG}_k} & \mathcal{J}_{mm}^{\mathrm{DG}_0\times\mathrm{DG}_0} & \mathcal{J}_{mf}^{\mathrm{DG}_0\times\mathrm{CG}_k}\\ \mathcal{J}_{fm}^{\mathrm{CG}_k\times\mathrm{CG}_k} & \mathcal{J}_{fm}^{\mathrm{CG}_k\times\mathrm{DG}_0} & \mathcal{J}_{ff}^{\mathrm{CG}_k\times\mathrm{CG}_k}\end{bmatrix}\begin{Bmatrix}p_{m,h}^{\mathrm{CG}_k}\\ p_{m,h}^{\mathrm{DG}_0}\\ p_{f,h}^{\mathrm{CG}_k}\end{Bmatrix} = \begin{Bmatrix}\ell_m^{\mathrm{CG}_k}\\ \ell_m^{\mathrm{DG}_0}\\ \ell_f^{\mathrm{CG}_k}\end{Bmatrix}. \tag{47}$$

This formulation makes the EG methodology easily implementable in any existing DG codes. Matrices and vectors are built by FEniCS form compiler (Alnaes et al., 2015). The block structure is setup using multiphenics toolbox (Ballarin and Rozza, 2019). Random field of permeability ($\boldsymbol{k_m}$) is populated using SciPy package (Jones et al., 2001). β, penalty parameter, is set at 1.1 and 1.0 for DG and EG methods, respectively.

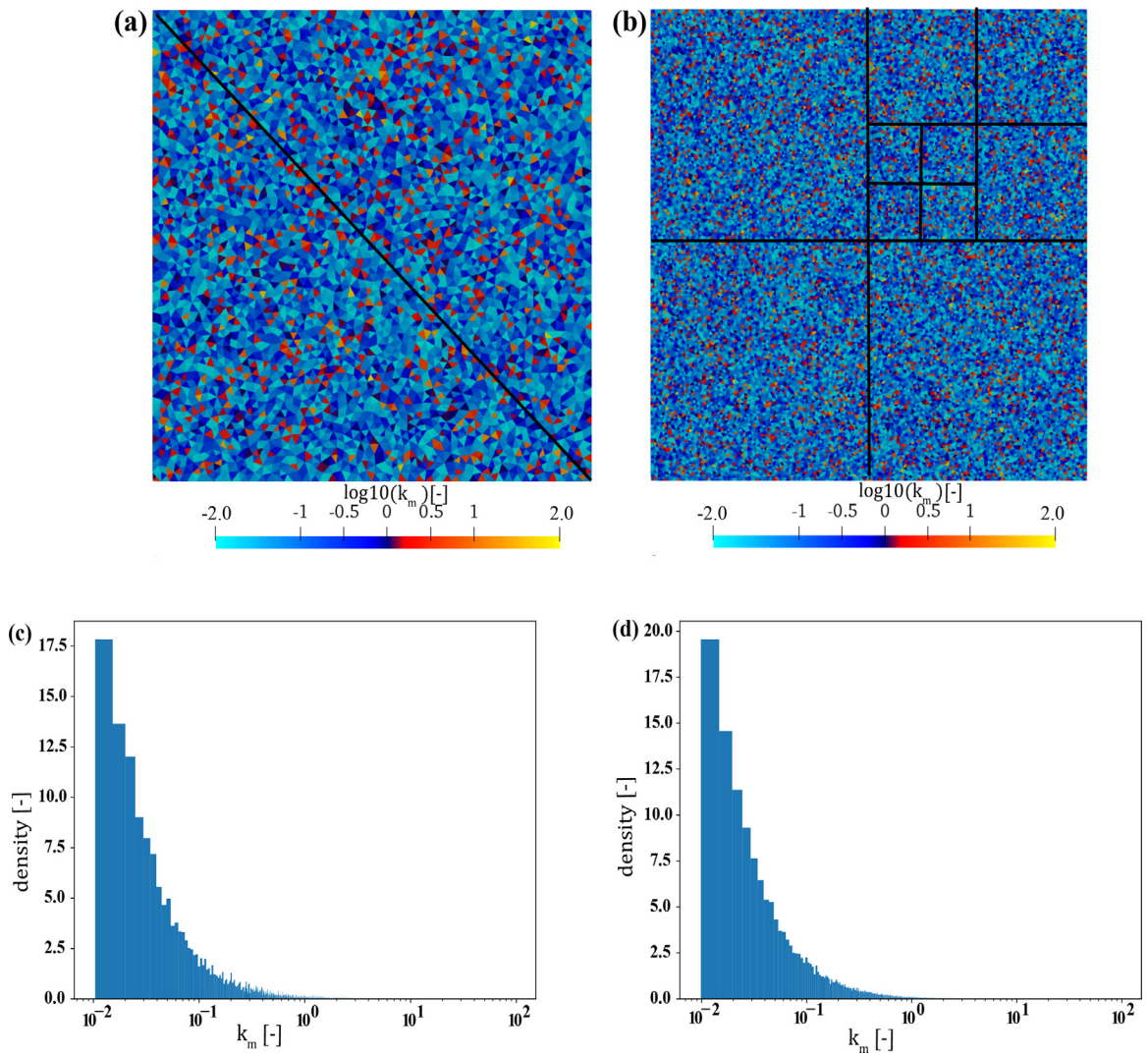

Fig. 14. Low $\boldsymbol{k_m}$ case: k_m distribution of: (**a**) quarter five-spot ($n_e = 6,568$), (**b**) regular fracture network ($n_e = 26,952$) examples, histogram of $\boldsymbol{k_m}$ of (**c**) quarter five-spot, and (**d**) regular fracture network examples.

Remark 4. We note that CG, DG, and EG methods are based on Galerkin method, which could be extended to consider adaptive meshes that contain hanging nodes. In addition, there are various advanced development for each methods to enhance the efficiency, including variable approximation order techniques. Especially, for EG method, an adaptive enrichment, i.e., the piecewise-constant functions only added to the elements where the sharp material discontinuities (e.g., between matrix and fracture domains) are observed, can be developed. However, in our following numerical examples, we focus on the classical form of each methods for the comparison by simulating the proposed mixed dimensional approach for modeling fractures.

3. Numerical examples

We illustrate the capability of the EG method using seven numerical examples. We begin with an analysis of the error convergence rate between the EG and DG methods to verify the developed block structure in the mixed-dimensional setting. We also investigate the EG performance in modeling the quarter five-spot pattern and handling the fracture tip in the immersed fracture geometry. Next, we test the EG method in a regular fracture network with and without a heterogeneity in matrix permeability input. Lastly, we apply time-dependent problems for two three-dimensional geometries; the first one represents the case where fractures are orthogonal to the axes, and another represents geometry where fractures are given with arbitrary orientations with their interactions in a three-dimensional domain.

3.1. Error convergence analysis

To verify the implementation of the proposed block structure utilized to solve the mixed-dimensional model using the EG method, we illustrate the error convergence rate of the EG method and compare this value with the DG method. The example used in this analysis is adapted from Antonietti et al. (2019). We take $\Omega = [0,1]^2$, and choose the exact solution in the matrix, Ω, and fracture, $\Gamma = \{(x,y) \in \Omega : x + y = 1\}$, as:

$$\begin{cases} p_m = e^{x+y} & \text{in } \Omega_1, \\ p_m = \dfrac{e^{x+y}}{2} + \left(\dfrac{1}{2} + \dfrac{3a_f}{k_f^n\sqrt{2}}\right)e & \text{in } \Omega_2, \\ p_f = e\left(1 + \sqrt{2}\dfrac{a_f}{k_f^n}\right) & \text{in } \Gamma. \end{cases} \tag{48}$$

By choosing $\boldsymbol{k_m} = \boldsymbol{I}$, (48) satisfies the system of equations, (1), (9), (15), and (16), presented in the methodology section with sink/source terms,

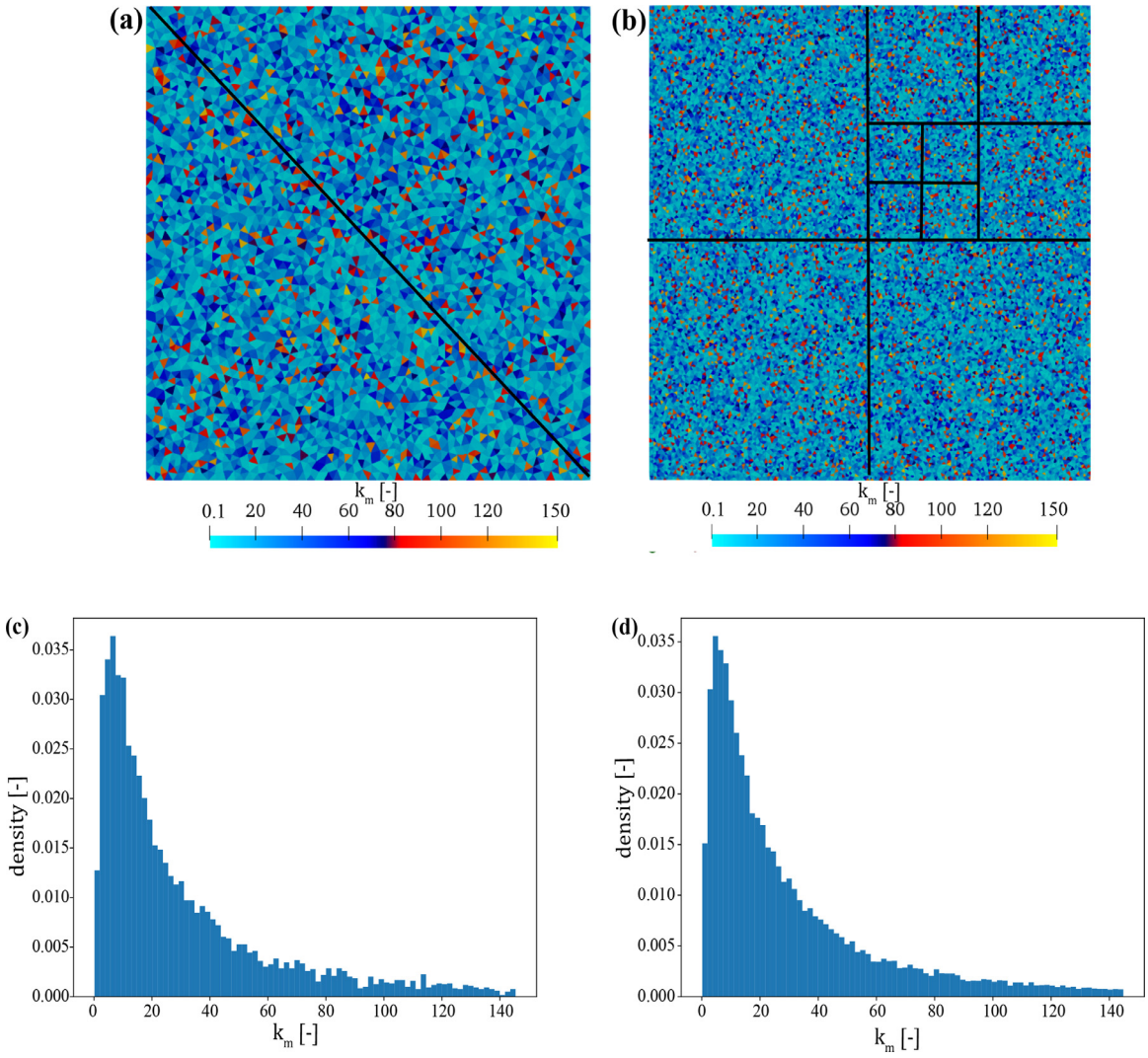

Fig. 15. High $\boldsymbol{k_m}$ case: k_m distribution of: (**a**) quarter five-spot ($n_e = 6,568$), (**b**) regular fracture network ($n_e = 26,952$) examples, histogram of $\boldsymbol{k_m}$ of (**c**) quarter five-spot, and (**d**) regular fracture network examples.

g, as follows:

$$\begin{cases} g_m = -2e^{x+y} & \text{in } \Omega_1, \\ g_m = -e^{x+y} & \text{in } \Omega_2, \\ g_f = \dfrac{e}{\sqrt{2}} & \text{in } \Gamma, \end{cases} \tag{49}$$

All other physical parameters are set to one, and the homogeneous boundary conditions are applied to all boundaries. The geometry used in this analysis and the illustration of the exact solution are presented in Fig. 5a-b, respectively.

We calculate L^2 norm of the difference between the exact solution, p, and approximated solution, p_h, and the results are presented in Fig. 5c-d for matrix and fracture domains, respectively. For both matrix and fracture domains, the EG and DG methods provide the expected convergence rate of two and three for polynomial degree approximation, k, of one and two, respectively (Antonietti et al., 2019; Babuska, 1973).

3.2. Quarter five-spot example

This numerical example tests the EG method performance in an injection/production setting using five-spot pattern, and we adopt this example from Chave et al. (2018), Antonietti et al. (2019). The five-spot pattern, where one injection well is located in the middle and four producers are located at each corner of the square, is commonly used in underground energy extraction Chen et al. (2006). Due to the symmetry of this geometry, only a quarter of the domain ($\Omega = [0,1]^2$) is simulated. The injection well is located at (0,0), and the production well is located at (1,1). We place the fracture with $a_f = 0.0005$ at $\Gamma = \{(x,y) \in \Omega : x + y = 1\}$. The geometry, boundary conditions, and mesh with $h = 1.2 \times 10^{-1}$ applied in this analysis are shown in Fig. 6.

The following source term is applied to the entire matrix domain including the injection and production wells:

$$g_m(x,y) = 10.1 \tan\left(200\left(0.2 - \sqrt{x^2+y^2}\right)\right) - 10.1 \tanh\left(200\left(0.2 - \sqrt{(x-1)^2+(y-1)^2}\right)\right). \tag{50}$$

To investigate the effect of fracture conductivity, we perform two simulations using different fracture conductivity inputs. (i) We choose, $\boldsymbol{k_m} = \boldsymbol{I}$, $k_f^n = 1$, and $\boldsymbol{k_f^T} = 100\boldsymbol{I}$ for the permeable fracture case. (ii) We assume the fracture is impermeable and set $\boldsymbol{k_m} = \boldsymbol{I}$, $k_f^n = 1 \times 10^{-2}$, and $\boldsymbol{k_f^T} = \boldsymbol{I}$. All of the remaining physical parameters are set to one.

Results of two cases are presented in Fig. 7a-b for the pressure value and Fig. 7c-d for the pressure profile along $x = y$ line. The pressure profile of the permeable fracture case is smoothly decreasing from the injection well towards the production well. The pressure profile of the im-

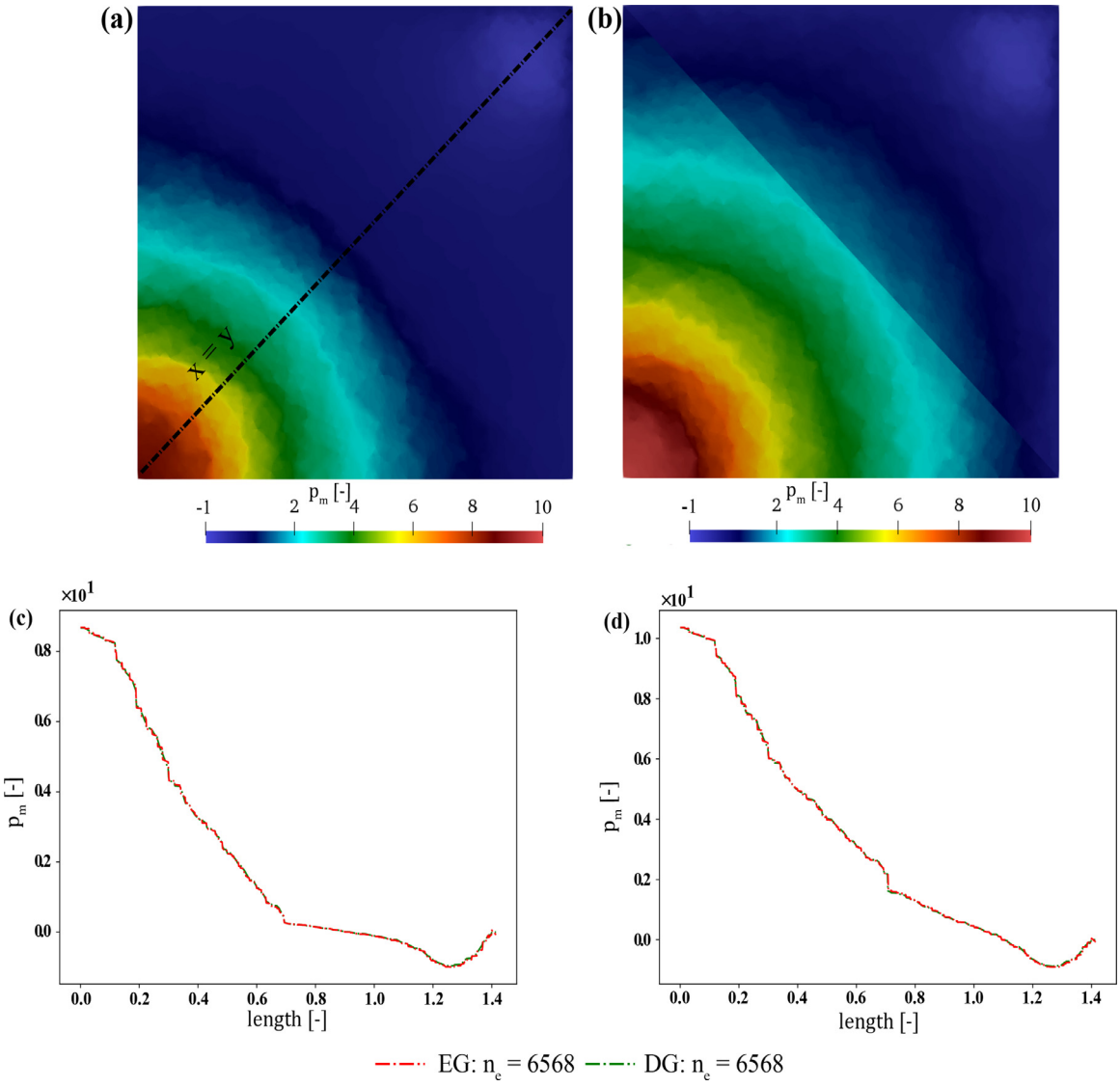

Fig. 16. The p_m solution of heterogeneous quarter five-spot example (low $\boldsymbol{k_m}$): (**a**) permeable fracture, (**b**) impermeable fracture cases, p_m plot along $x = y$ line of (**c**) permeable fracture, and (**d**) impermeable fracture cases. All of the results obtained from the EG and DG methods approximately overlap.

permeable fracture case, on the other hand, illustrates a jump across the fracture interface. These findings comply with the results of the previous studies (Chave et al., 2018; Antonietti et al., 2019). Our results converge to the reference solution as the h is reduced from $h = 1.2 \times 10^{-1}$ to $h = 7.2 \times 10^{-2}$. Note that (Antonietti et al., 2019) perform these numerical experiments using the second-order DG method with $h = 7.5 \times 10^{-2}$ on polytopic grids (Antonietti et al., 2019). There is no significant difference between the EG and DG results for both h values (Fig. 7c-d).

3.3. Immersed fracture example

The numerical examples discussed so far contain a fracture that cut through the matrix domain. To test the EG discretization capability in the immersed fracture setting, we adopt this example from Angot et al. (2009). Since we assume that the fracture tip is substantially small, there is no fluid mass transfer between the matrix and fracture domains across the fracture tip, see A' in Fig. 8. Hence, the fracture boundary, Λ_h^N, that intersects with the bulk matrix material internal boundary, $\mathcal{E}_h^0$, is enforced with no-flow boundary condition, $q_{fN} = 0$.

In this example, we take the bulk matrix, $\Omega = [0, 1]^2$, and the fracture with $a_f = 0.01$, $\Gamma = \{(x, y) \in \Omega : x = 0.5, y \geq 0.5\}$. We perform three simulations using different fracture conductivity inputs; (i) we assume $\boldsymbol{k_m} = \boldsymbol{I}$, $k_f^n = 1 \times 10^2$, and $\boldsymbol{k_f^T} = 1 \times 10^6 \boldsymbol{I}$ for the permeable fracture case, and its geometry and boundary conditions are presented in Fig. 8a. (ii) The partially permeable fracture case utilizes $\boldsymbol{k_m} = \boldsymbol{I}$, $k_f^n = 1 \times 10^2$, and $\boldsymbol{k_f^T} = 1 \times 10^2 \boldsymbol{I}$. This case geometry and boundary conditions are illustrated in Fig. 8b. (iii) Impermeable fracture, geometry and boundary conditions are shown in Fig. 8c, and it uses $\boldsymbol{k_m} = \boldsymbol{I}$, $k_f^n = 1 \times 10^{-7}$, and $\boldsymbol{k_f^T} = 1 \times 10^{-7} \boldsymbol{I}$. All other physical parameters are equal to one. Example of mesh that contains $n_e = 272$ is shown in Fig. 8d.

In Fig. 9, the values of p_m with $n_e = 1,741$ for all cases are presented. The pressure plot along $y = 0.75$ is presented in Fig. 10. The permeable and partially permeable fracture cases illustrate the continuity of the pressure while the impermeable fracture case shows the jump across the fracture interface. Our results converge ($n_e = 272$, $n_e = 1,741$, and $n_e = 6,698$) to the solutions provided by Angot et al. (2009). Moreover, the EG and DG methods provide similar results. Note that the reference solutions are performed on the finite volume method with 65,536 control volumes.

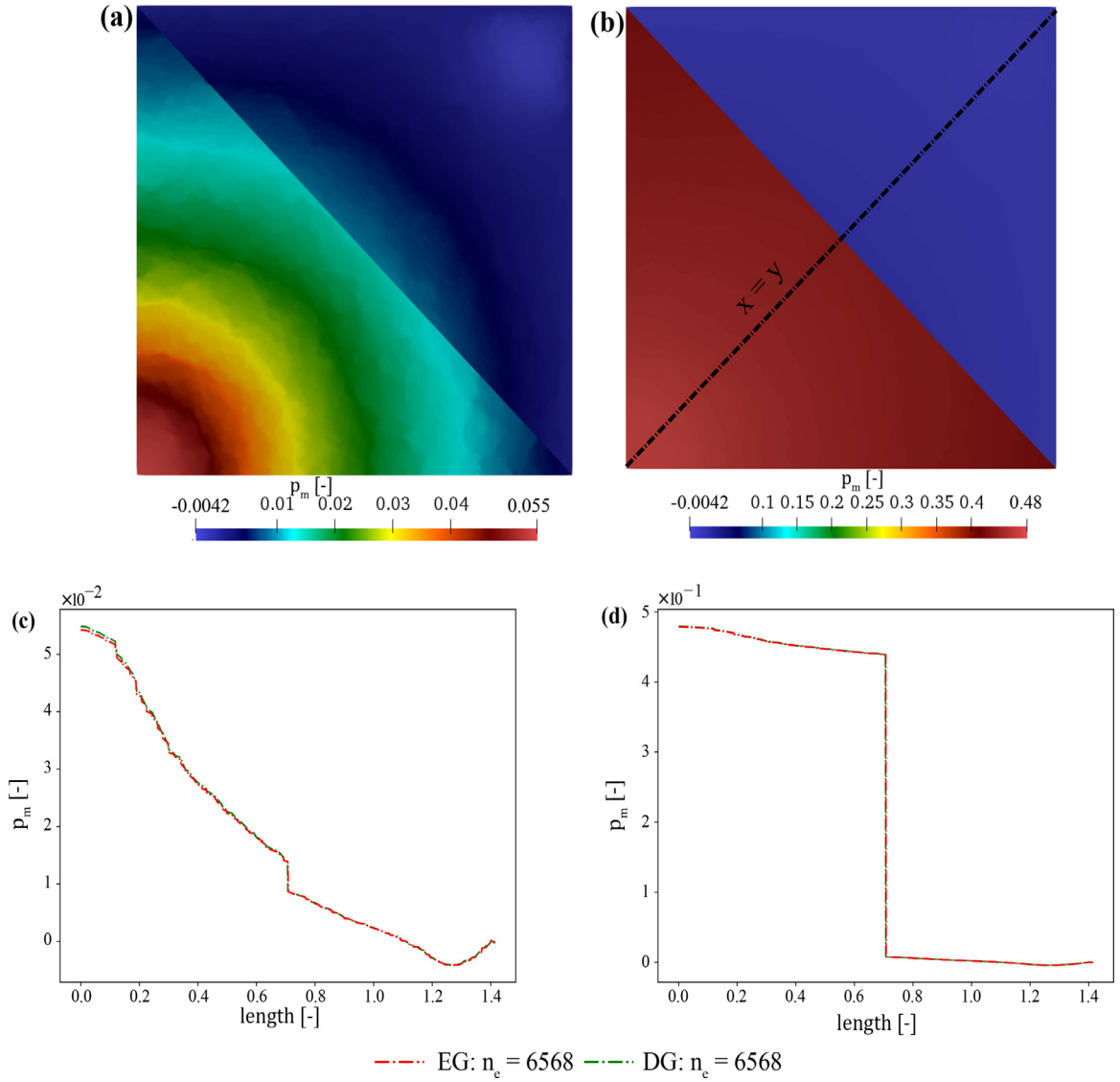

Fig. 17. The p_m solution of heterogeneous quarter five-spot example (high $\boldsymbol{k_m}$): (**a**) permeable fracture, (**b**) impermeable fracture cases, p_m plot along $x = y$ line of (**c**) permeable fracture, and (**d**) impermeable fracture cases. All of the results obtained from the EG and DG methods approximately overlap.

3.4. Regular fracture network example

We increase the complexity of the problem by increasing the number of fractures as shown in Flemisch et al. (2018). This example, however, is called regular fracture network since all fractures are orthogonal to the axes (x or y). The geometry used in this example was utilized by Geiger et al. (2013) for analyzing multi-rate dual-porosity model. Details for model geometry and boundary conditions are shown in Fig. 11a. We set $\boldsymbol{k_m} = \boldsymbol{I}$ for all the matrix domain, $\Omega = [0, 1]^2$, and $a_f = 1 \times 10^{-4}$ for all fractures, Γ. Two fracture conductivity inputs are used; (i) we choose $k_f^n = 1 \times 10^4$ and $\boldsymbol{k}_f^T = \times 10^4 \boldsymbol{I}$ for the permeable fracture case. (ii) For the impermeable fracture case, we assume $k_f^n = 1 \times 10^{-4}$, and $\boldsymbol{k}_f^T = 1 \times 10^{-4} \boldsymbol{I}$. All of the remaining physical parameters are set to one. Example of mesh that contains $n_e = 184$ is shown in Fig. 11d.

The p_m results of the permeable and impermeable fractures are presented in Fig. 11b-c, respectively. The permeable fracture case shows the smooth p_m profile while the impermeable fracture case clearly illustrates the jump of p_m across the fracture interface. These results are the same as the reference solutions provided by Flemisch et al. (2018).

Figs. 12 a-b present the pressure plots along the lines $y = 0.7$ and $x = 0.5$ of the permeable fracture case. The pressure plot along $(x = 0.0, y = 0.1)$ to $(x = 0.9, y = 1.0)$ line of impermeable fracture case is shown in Fig. 12c. Our results using $n_e = 184$, $n_e = 382$, $n_e = 2,046$, and $n_e = 26,952$ converge to the reference solutions provided by Flemisch et al. (2018). The reference solution is simulated based on finite volume method with equi-dimensional setting, and it contains 1,175,056 elements Flemisch et al. (2018).

Besides the evaluation of pressure results, we also investigate the flux calculated at face A' (see Fig. 11a) as follows:

$$\text{flux} = -\sum_{e \in \text{A}'} \int_e \frac{\boldsymbol{k}_m}{\mu} (\nabla p_m - \rho \mathbf{g}) \cdot \boldsymbol{n} \, dS \text{ on A}', \tag{51}$$

As presented in Fig. 13, the difference between each n_e case is insignificant, i.e. the different between $n_e = 26,952$ and $n_e = 184$ cases is less than 1%. Furthermore, there is no difference between the EG and DG methods. The DOF comparison between EG and DG methods is shown in Table 1. The EG method requires the DOF (in the matrix domain) approximately half of that of the DG method. Note that the DOF in the fracture domain is the same because we discretize the fracture domain using the CG method.

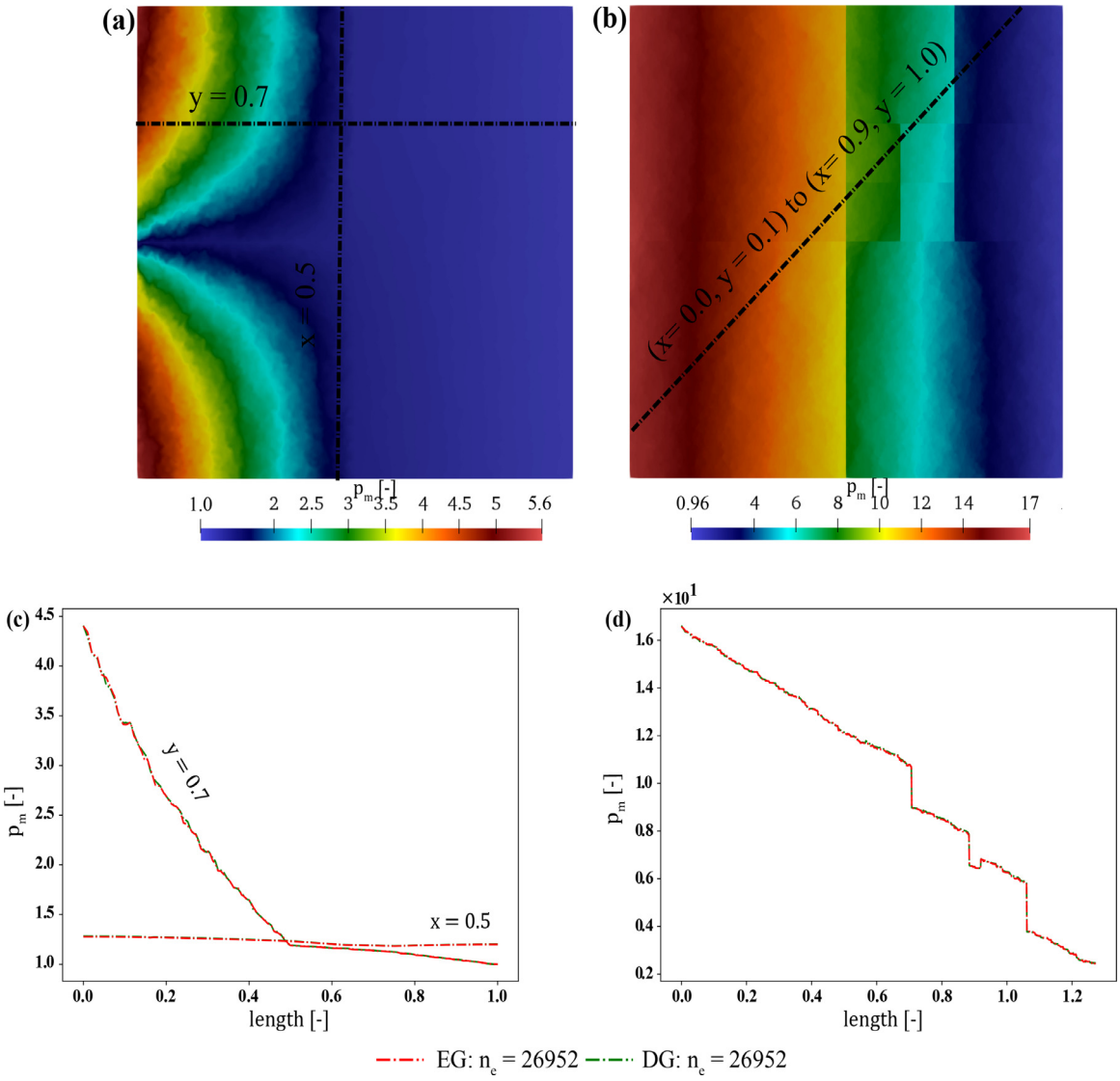

Fig. 18. The p_m solution of heterogeneous regular fracture network example (low $\boldsymbol{k_m}$): (**a**) permeable fracture, (**b**) impermeable fracture cases, p_m plot along (**c**) $y = 0.7$ and $x = 0.5$ lines of permeable fracture case, and (**d**) $(x = 0.0, y = 0.1)$ to $(x = 0.9, y = 1.0)$ line of impermeable fracture case.

Table 1
Degrees of freedom (DOF) comparison between EG and DG methods of regular fracture network example.

n_e	EG		DG	
	matrix domain	fracture domain	matrix domain	fracture domain
26,952	40,629	13,677	80,856	13,677
2,046	3,123	1,077	6,138	1,077
382	595	213	1,146	213
184	293	109	552	109

3.5. The heterogeneous in bulk matrix permeability example

The numerical examples presented so far only consider an homogeneous matrix permeability value. In this section, we examine the capability of the EG method in handling the discontinuity not only between the fracture and matrix domains but also within the matrix domain (e.g. Nick and Matthai, 2011b) by employing the heterogeneous permeability in the bulk matrix. We adapt the quarter five-spot as in Section 3.2 and regular fracture network as in Section 3.4. We choose the finest mesh from both examples to test the EG method capability compared to that of the DG method in handling the sharp discontinuity between the maximum number of interfaces. The geometries, boundary conditions, and input parameters are utilized as Sections 3.2 and 3.4 except for the $\boldsymbol{k_m}$ value.

In this study, $\boldsymbol{k_m} = k_m \boldsymbol{I}$, k_m value is randomly provided value for each cell. We will distinguish in particular two different cases, named low $\boldsymbol{k_m}$ case and high $\boldsymbol{k_m}$ case in the following. The low $\boldsymbol{k_m}$ case is characterized by a log-normal distribution with average $\bar{k_m} = 1.0$, variance $\mathrm{var}(k_m) = 40$, limited to minimum value $k_{m\,\min} = 1.0 \times 10^{-2}$, and maximum value $k_{m\,\max} = 1.0 \times 10^{2}$. The high $\boldsymbol{k_m}$ case uses $\bar{k_m} = 30.0$, $\mathrm{var}(k_m) = 90$, $k_{m\,\min} = 1.0 \times 10^{-1}$, and $k_{m\,\max} = 1.5 \times 10^{2}$. This heterogeneous fields for both examples are populated using SciPy package (Jones et al., 2001) as shown in Figs. 14 and 15 for low $\boldsymbol{k_m}$ and high $\boldsymbol{k_m}$ cases, respectively.

3.5.1. Quarter five-spot example

The results for the low $\boldsymbol{k_m}$ case with permeable ($k_f^n = 1$ and $\boldsymbol{k_f^T} = 100\boldsymbol{I}$) and impermeable ($k_f^n = 1 \times 10^{-2}$ and $\boldsymbol{k_f^T} = \boldsymbol{I}$) fractures are illustrated in Fig. 16. In general, the p_m profile from the two cases are more disperse than the homogeneous $\boldsymbol{k_m}$ setting. The EG and DG methods provide similar results, with $n_e = 6,568$ and $h = 7.2 \times 10^{-2}$. The discussions

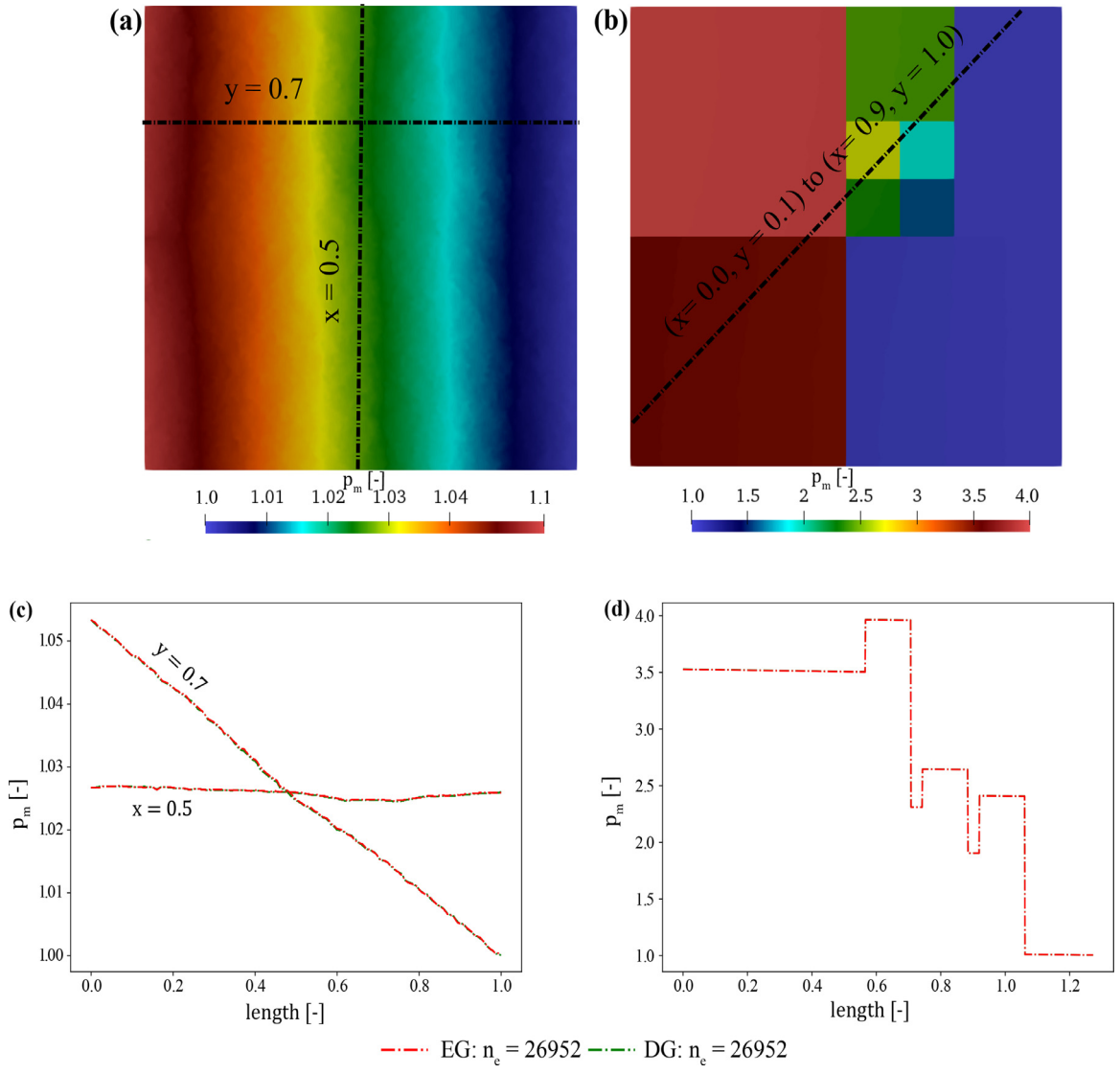

Fig. 19. The p_m solution of heterogeneous regular fracture network example (high $\boldsymbol{k_m}$): (**a**) permeable fracture, (**b**) impermeable fracture cases, p_m plot along (**c**) $y = 0.7$ and $x = 0.5$ lines of permeable fracture case, and (**d**) $(x = 0.0, y = 0.1)$ to $(x = 0.9, y = 1.0)$ line of impermeable fracture case.

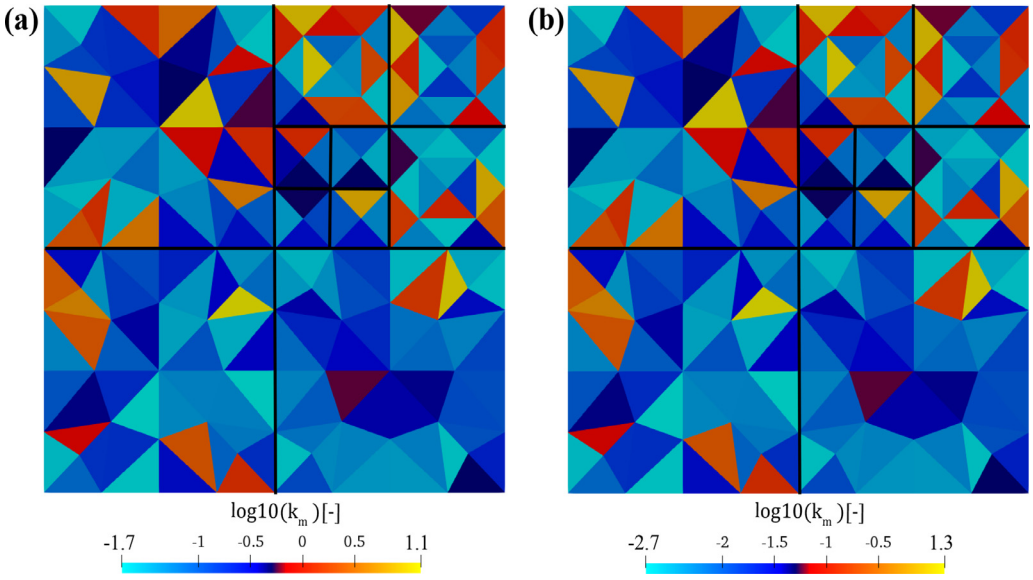

Fig. 20. Heterogeneous and anisotropy $\boldsymbol{k_m}$ case of the regular fracture network ($n_e = 184$) example: (**a**) diagonal value of $\boldsymbol{k_m}$ and (**b**) off-diagonal value of $\boldsymbol{k_m}$.

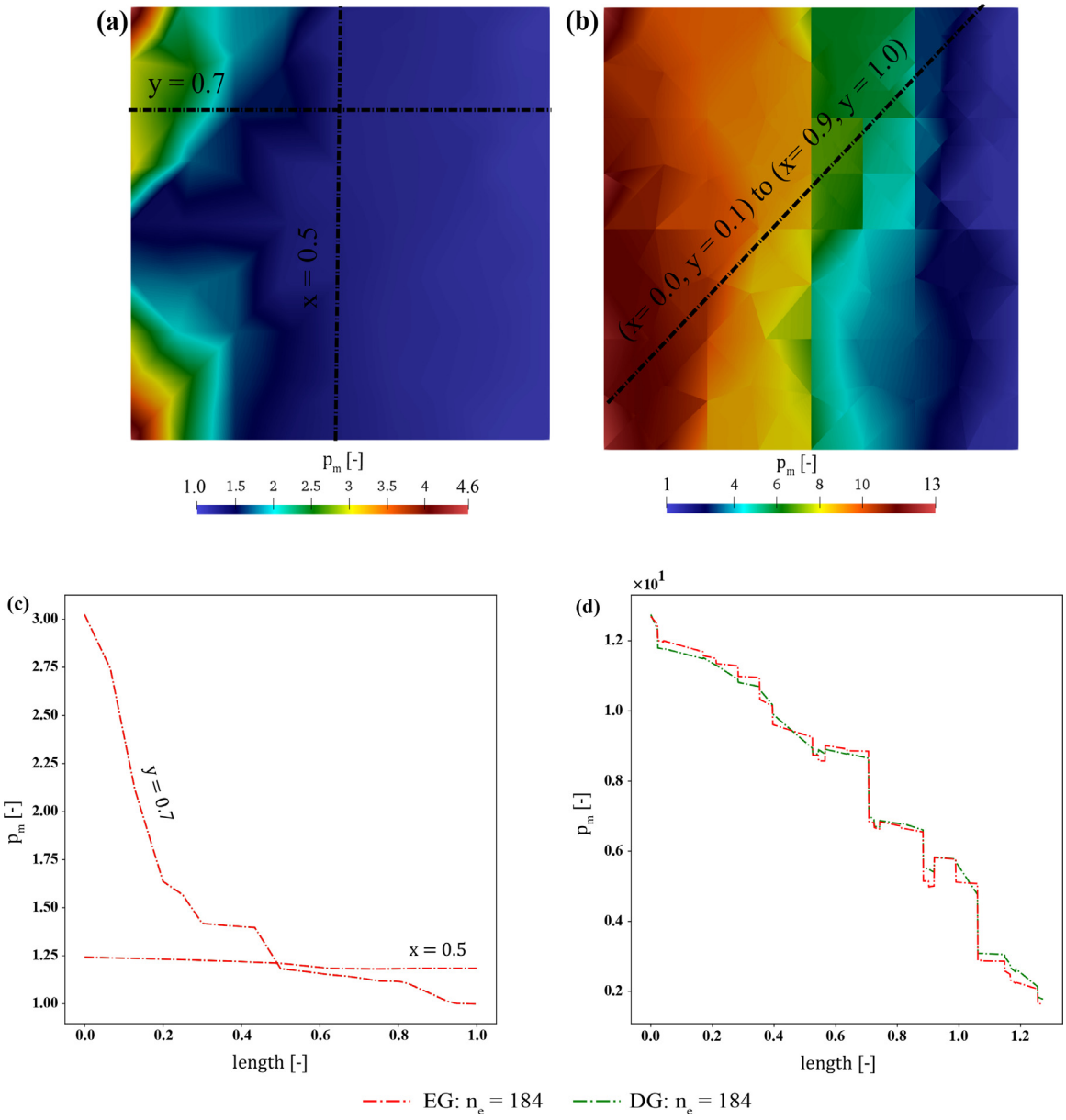

Fig. 21. The p_m solution of heterogeneous and anisotropy $\boldsymbol{k_m}$ in regular fracture network example: (**a**) permeable fracture, (**b**) impermeable fracture cases, the p_m plot along (**c**) $y = 0.7$ and $x = 0.5$ lines of permeable fracture case, and (**d**) $(x = 0.0, y = 0.1)$ to $(x = 0.9, y = 1.0)$ line of impermeable fracture case.

regarding permeable and impermable fracture settings are provided as follows:

1. *Low $\boldsymbol{k_m}$ with permeable fracture* result illustrates the approximately smooth p_m solution because the $\bar{k_m} = 1.0$ is equal to k_f^n. The plot along $x = y$ line, as expected, shows p_m gradually decreases from the injection well to the production well. This result complies with that of the homogeneous $\boldsymbol{k_m}$ setting.
2. *Low $\boldsymbol{k_m}$ with impermeable fracture* result and the plot along $x = y$ line exhibit a little jump of p_m across the fracture interface. This behavior is different from the homogeneous $\boldsymbol{k_m}$ setting since $k_{m\,\min} = k_f^n$, which lead to the less permeability contrast between the fracture and matrix domains.

The results for the high $\boldsymbol{k_m}$ case with permeable and impermeable fractures are presented in Fig. 17. Using $n_e = 6,568$, the EG and DG results are approximately the same. The observations concerning the fracture permeability are presented below:

1. *High $\boldsymbol{k_m}$ with permeable fracture* displays a jump across the fracture domain because $\boldsymbol{k_m}$ around the fracture on the plotting line is higher than k_f^n; as a result, the fracture interface acts like a flow barrier. The plot along $x = y$ line supports this observation as p_m jumps across the fracture interface.
2. *High $\boldsymbol{k_m}$ with impermeable fracture* illustrates a huge jump across the fracture interface, as can be observed from the p_m plot along $x = y$ line, since $\boldsymbol{k_m}$ is much higher than k_f^n. The p_m variation is less pronounced compared to the low $\boldsymbol{k_m}$ one, see Figs. 7b (homogeneous) and 16b (heterogeneous), because the fluid flow is blocked by the fracture interface (sharp material discontinuity).

3.5.2. Regular fracture network example

The pressure results of the low $\boldsymbol{k_m}$ case between the permeable ($k_f^n = 1 \times 10^4$ and $\boldsymbol{k_f^T} = \times 10^4 \boldsymbol{I}$) and impermeable ($k_f^n = 1 \times 10^{-4}$ and $\boldsymbol{k_f^T} = 1 \times 10^{-4} \boldsymbol{I}$) fractures are illustrated in Fig. 18. Similar to the five-spot example, the EG and DG results are similar with $n_e = 26,952$, and p_m results are more dispersive than the homogeneous $\boldsymbol{k_m}$ setting as shown in

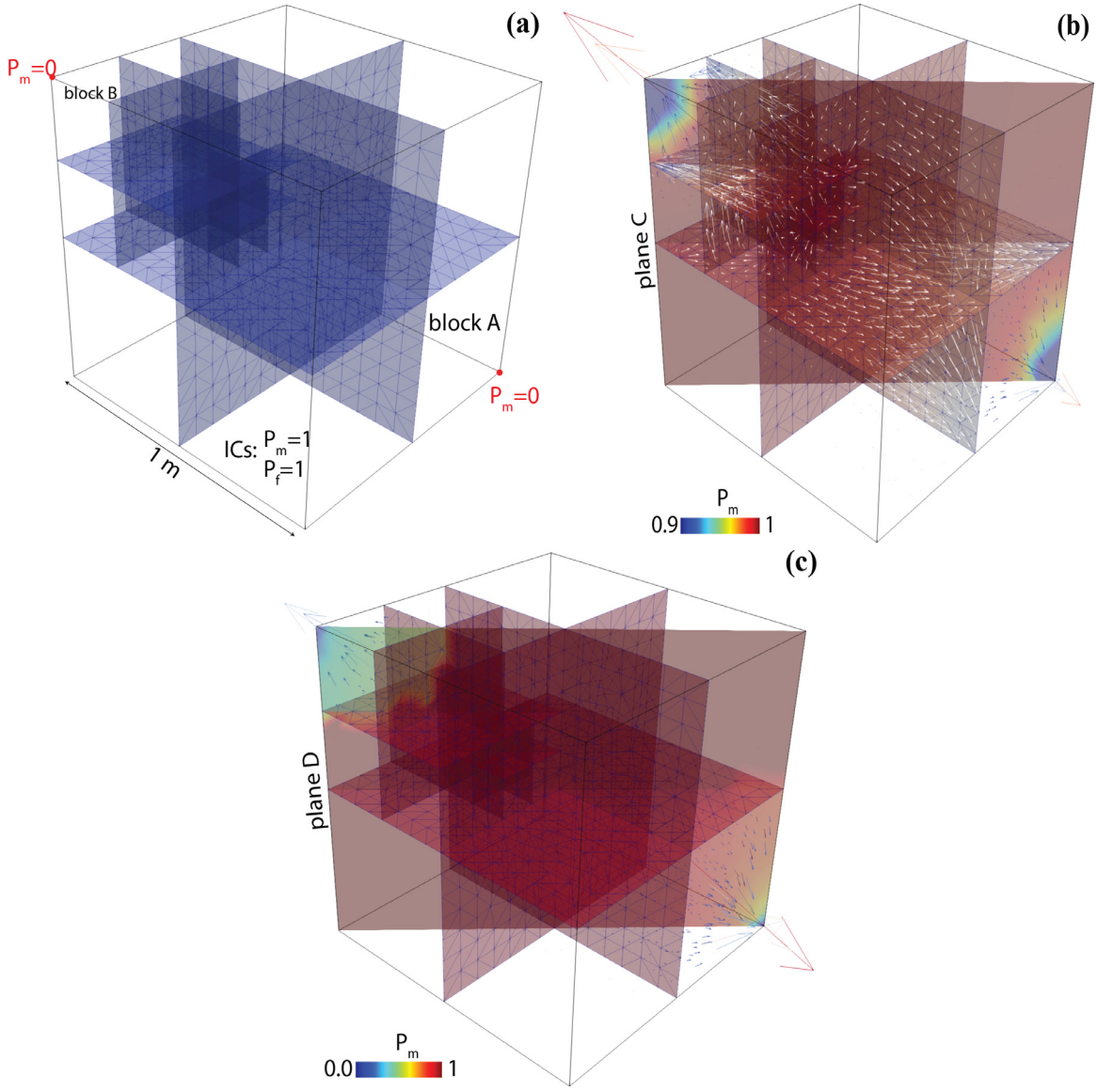

Fig. 22. Three-dimensional regular fracture network. The illustrated surfaces with edges (blue in **a** and red in **b** and **c**) indicate the fractures. (**a**) geometry and initial/boundary conditions are presented. p_m is enforced as zero on two corner points shown in red and no-flow condition is applied to all boundaries. Initial conditions (ICs) for p_m and p_f are set as one. (**b**) presents pressure solution on plane C, p_m, matrix velocity, $\boldsymbol{v_m}$, and fracture velocity, $\boldsymbol{v_f}$, with the permeable fracture (case i), (**c**) presents p_m on plane D, $\boldsymbol{v_m}$, and $\boldsymbol{v_f}$ with impermeable fracture cases (case ii). Note that the matrix pressure is only shown in the cross section between the far two edges of the model. (For interpretation of the references to colour in this figure legend, the reader is referred to the web version of this article.)

Fig. 19a-b. The discussions regarding permeable and impermable fracture settings are provided as follows:

1. *Low $\boldsymbol{k_m}$ with permeable fracture* illustrates the fracture dominate flow regime, even though $\bar{k_m} = 1.0$, $k_{m\min}$ is set to 1.0×10^{-2}, which is much less than k_f^n. This setting reduces the impact of the matrix domain. p_m plot along $y = 0.7$ and $x = 0.5$ lines support this observation by showing the high pressure gradient in the matrix domain, but p_m becomes much less varied when entering the fracture domain.
2. *Low $\boldsymbol{k_m}$ with impermeable fracture* also presents the fracture dominate flow regime because $k_f^n = 1 \times 10^{-4}$, which is less than $k_{m\min} = 1.0 \times 10^{-2}$. Therefore, the flow in the matrix is blocked by the fracture domain. The plot along $(x = 0.0, y = 0.1)$ to $(x = 0.9, y = 1.0)$ line illustrates jumps across the fracture domain, which is supporting our observation.

The results for the high $\boldsymbol{k_m}$ case with permeable and impermeable fractures are presented in Fig. 19. With $n_e = 26,952$, the EG and DG results are approximately the same. The observations concerning the fracture permeability are presented below:

1. *High $\boldsymbol{k_m}$ with permeable fracture* shows that the matrix domain gains more momentum comparing to the low $\boldsymbol{k_m}$ case. p_m plot along $y = 0.7$ and $x = 0.5$ lines illustrates also approximately linear reduction along the matrix domain, while pressure is almost constant in the fracture domain.
2. *High $\boldsymbol{k_m}$ with impermeable fracture* clearly presents the fracture domain dominate the flow because k_f^n is much less than the $\boldsymbol{k_m}$. Hence, the flow is blocked by the fractures. The plot along $(x = 0.0, y = 0.1)$ to $(x = 0.9, y = 1.0)$ line support this observation by illustrating multiple jumps across the fracture domain and no p_m variation inside each matrix block.

3.6. The heterogeneous and anisotropy in bulk matrix permeability example

This section illustrates the comparison between the p_m solutions of EG and DG methods using the heterogeneous and anisotropic $\boldsymbol{k_m}$. In con-

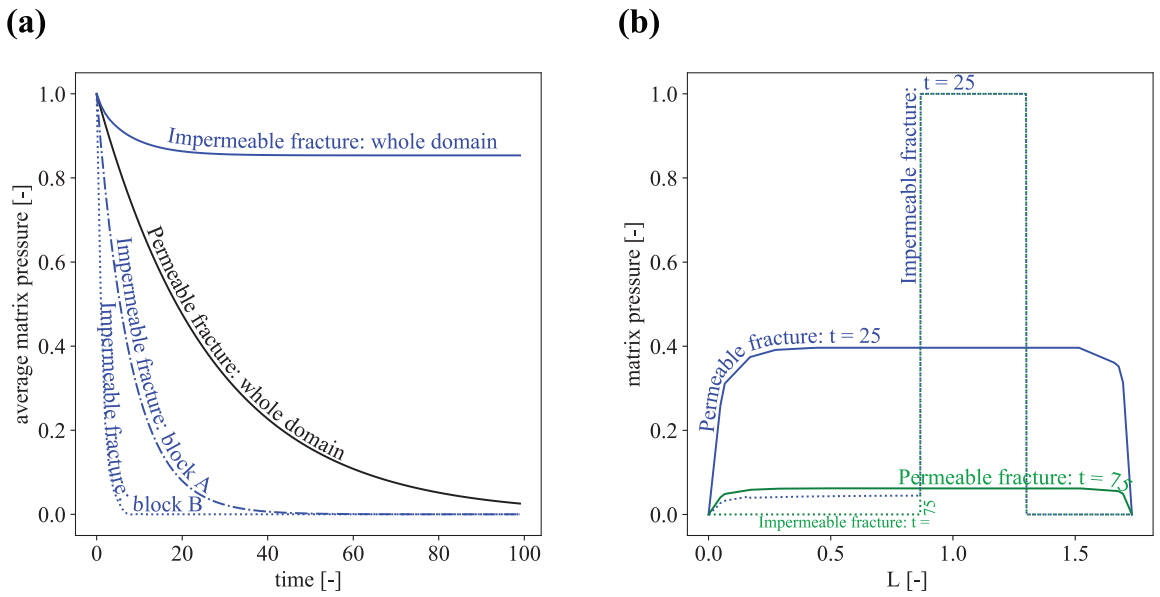

Fig. 23. Comparison of (**a**) the average p_m in the whole domain and blocks A and B, and (**b**) the p_m profiles for t=25 and t=75 along $(x = 0.0, y = 0.0, z = 0.0)$ to $(x = 1.0, y = 1.0, z = 1.0)$ line.

trast with the previous example, we utilize the coarsest mesh ($n_e = 184$) from the regular fracture network example. The matrix permeability heterogeneity, k_m, is generated with the same specification as the low $\boldsymbol{k_m}$ case in the previous section. However, in this study, the off-diagonal terms of (13) are not zero, and the $\boldsymbol{k_m}$ of each element is defined as follows:

$$\boldsymbol{k_m} := \begin{bmatrix} k_m & 0.1k_m \\ 0.1k_m & k_m \end{bmatrix}, \tag{52}$$

The generated heterogeneous field is shown in Fig. 20a-b for both diagonal and off diagonal terms.

The pressure results of the low $\boldsymbol{k_m}$ case between the permeable ($k_f^n = 1 \times 10^4$ and $\boldsymbol{k_f^T} = \times 10^4 \boldsymbol{I}$) and impermeable ($k_f^n = 1 \times 10^{-4}$ and $\boldsymbol{k_f^T} = 1 \times 10^{-4} \boldsymbol{I}$) fractures are presented in Fig. 21. The results of EG and DG methods are approximately similar for both fracture permeability settings. These results illustrate that the EG method captures the discontinuities and allow using a coarse mesh to maintain accuracy.

3.7. The time-dependent problems

From this section, we consider time-dependent problem where c and ϕ_{mi} are nonzero (1)–(8). Besides, we extend the spatial domain to three-dimensional space to further illustrate the applicability of the proposed EG method. Here, the first example considers the geometry containing only the orthogonal fractures to the axes (x, y, or z), and the second example assumes the geometry with arbitrary orientated natural fractures. Note that we, here, present only the results of the EG method. The results of the DG method are comparable to those of the EG method.

3.7.1. Three-dimensional regular fracture network example.

In this example, we consider a three-dimensional domain, which is an analog of the two-dimensional case presented in Section 3.5.2. This domain contains a set of well-interconnected fractures and meshed with tetrahedral and triangular elements (for fractures) with $n_e = 9,544$. The fracture geometry is based on the example in Berre et al. (2020). The details of geometry with initial and boundary conditions illustrated in Fig. 22a.

Here, we consider two different scenarios: case i) permeable fracture case with $k_f^n = 1 \times 10^6$ and $\boldsymbol{k_f^T} = 1 \times 10^6 \boldsymbol{I}$; and case ii) impermeable fracture case with $k_f^n = 1 \times 10^{-12}$, and $\boldsymbol{k_f^T} = 1 \times 10^{-12} \boldsymbol{I}$. For both cases, we employ a permeable porous medium by setting $\boldsymbol{k_m} = [1.0, 1.0, 0.1]\boldsymbol{I}$, and all of the remaining physical parameters are set to one for the simplicity. The temporal domain is given as $\mathbb{T} = [0, 100]$ where an uniform time step size $\Delta t^n = 1$.

In Fig. 22b-c, the numerical results of the p_m, $\boldsymbol{v_m}$, and $\boldsymbol{v_f}$ for the permeable (case i) and impermeable fracture cases (case ii) at $t = 100$ are presented. A mere visual examination of these results already shows that the fracture permeability controls the flow field. For the permeable fracture case, the velocity at the corner of block B is higher than that on the opposite corner in block A as the fractures are closer to the open corner point in block B. For the impermeable fracture case the velocity at the corner of block B is lower than that on the opposite corner in block A since block A is larger than block B, and it can support flow for a longer time.

Similar behaviors of the pressure values are observed in Fig. 23a, where the average pressure values of the full domain and block A and B are plotted for $\mathbb{T} = [0, 100]$. It is clear that the average pressure in block B drops faster than in block A for the impermeable case. Moreover, Fig. 23b illustrates the value of p_m along $(x = 0.0, y = 0.0, z = 0.0)$ to $(x = 1.0, y = 1.0, z = 1.0)$ line at $t = 25$ and 75.

3.7.2. Algrøyna outcrop example

The final example is a three-dimensional fracture network built based on an outcrop map in Algrøyna, Norway (Fumagalli et al., 2019). The model has a size of 850 × 1400 × 600 m and contains 52 intersecting fractures (the model is described in detail in Berre et al., 2020). The finite element mesh is discretized by tetrahedral (rock matrix) with $n_e = 163,575$ and triangular elements (fractures) with $n_e = 329,080$. See Fig. 24a for more details. As shown in this figure Dirichlet boundary conditions are applied on two edges of the model to represent an injection and a production well. All other boundaries are considered as no-flow. The rock matrix and the fractures are considered permeable: $k_f^n = 1 \times 10^2$, m^2 $\boldsymbol{k_f^T} = 1 \times 10^2 \boldsymbol{I}$ m^2, and $\boldsymbol{k_m} = [1.0, 1.0, 0.1]\boldsymbol{I}$ m^2. All of the remaining physical parameters are set to one, and $\mathbb{T} = [0, 1 \times 10^6]$ sec using an uniform Δt^n of 1×10^5 sec.

Fig. 24b and c show the simulation results including the pressure field, the pressure iso-surfaces, and velocity vectors in the rock matrix at $t = 500,000$ sec. The pressure profiles along a line between two opposite corners of the model at different times are plotted in Fig. 24d. This example illustrates the applicability of the presented EG method

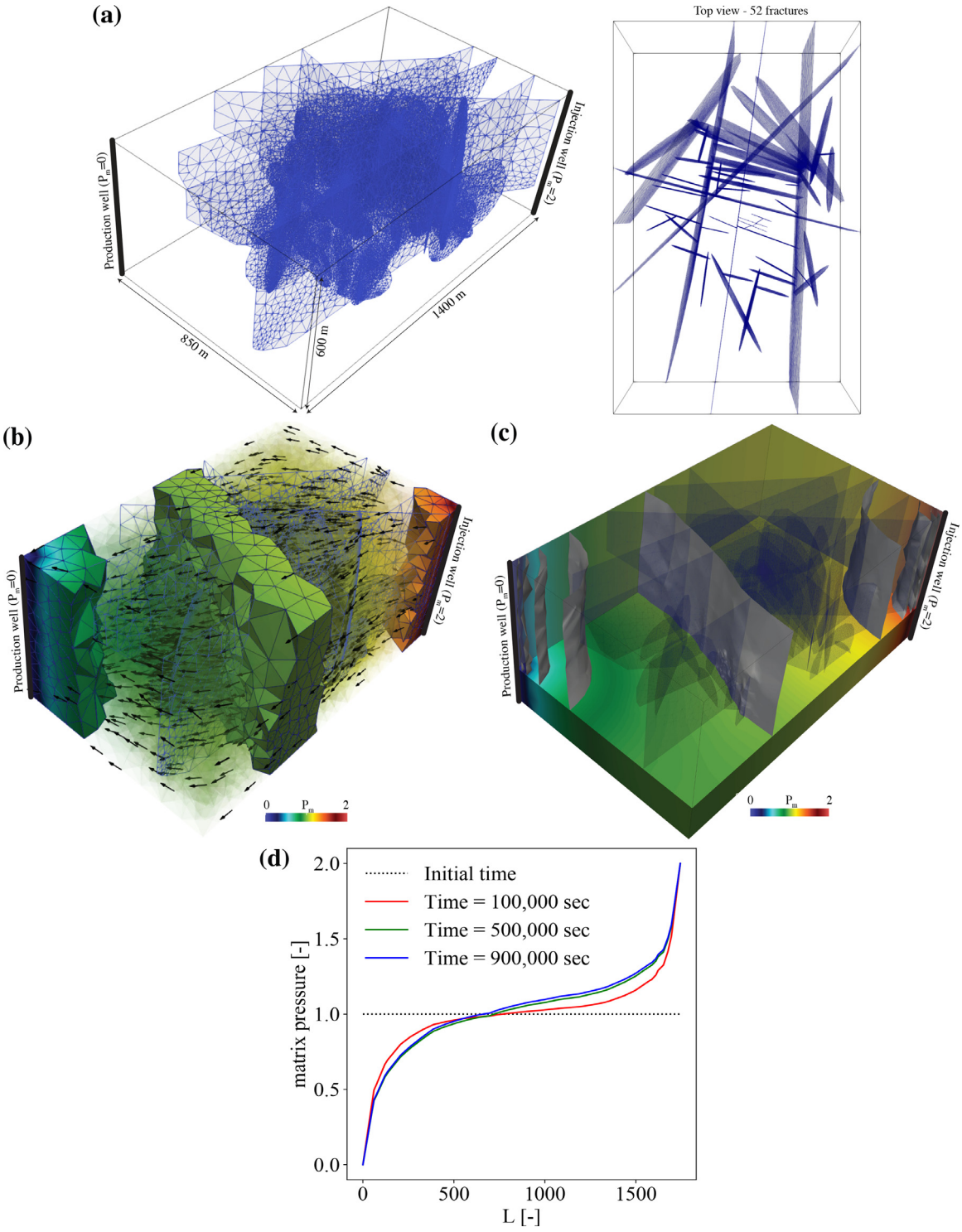

Fig. 24. Algrøyna outcrop example: (**a**) geometry and initial/boundary conditions (no-flow condition is applied to all boundaries (excepts the production and injection wells). Initial conditions (ICs) for p_m and p_f are set as one.), **b**) pressure solution, p_m, matrix velocity (in black arrow), $\boldsymbol{v_m}$, and fractures mesh, (**c**) p_m and its iso-surfaces shown in grey, and (**d**) pressure profiles along a line from the top of injection well to the bottom of production well.

for a complex three-dimensional fracture network with arbitrary orientations.

4. Conclusion

This study presents the EG discretization for solving a single-phase fluid flow in the fractured porous media using the mixed-dimensional approach. Our proposed method has been tested against several published benchmarks and subsequently assessed its performance in the test cases with the heterogeneous and anisotropic matrix permeability. Our results illustrate that the pressure solutions resulted from the EG and DG method, with the same mesh size, are approximately similar. Furthermore, the EG method enjoys the same benefits as the DG method; for instance, preserves local and global conservation for fluxes, can handle discontinuity within and between the subdomains, and has the optimal

error convergence rate. However, it has much fewer degrees of freedom compared to that of the DG method in its classical form. We note that this comparison can vary based on advanced developments of each method, e.g., a hybridized discontinuous Galerkin method or variable approximation orders. Besides, the results of the time-dependent problem for a three-dimensional geometry highlight the importance of correctly capturing the discontinuities with conductivity values, from barriers to highly-conductive fractures, present in geological media. This work can be extended to multiphysics problems, e.g., poroelastic and transport phenomena, and general form of the mixed-dimensional abstraction, i.e., coupled between d and $d - n$ dimensionality, where d and n are any integers and $d - n \geq 0$.

Declaration of Competing Interest

The authors declare that they have no known competing financial interests or personal relationships that could have appeared to influence the work reported in this paper.

CRediT authorship contribution statement

T. Kadeethum: Conceptualization, Formal analysis, Software, Validation, Writing - original draft. **H.M. Nick:** Conceptualization, Funding acquisition, Supervision, Writing - review & editing. **S. Lee:** Conceptualization, Formal analysis, Supervision, Validation. **F. Ballarin:** Conceptualization, Formal analysis, Software, Supervision, Validation, Writing - review & editing.

Acknowledgements

The research leading to these results has received funding from the Danish Hydrocarbon Research and Technology Centre under the Advanced Water Flooding program. The computations in this work have been performed with the multiphenics library Ballarin and Rozza (2019), which is an extension of FEniCS Alnaes et al. (2015) for multiphysics problems. We acknowledge developers and contributors to both libraries. FB also thanks Horizon 2020 Program for Grant H2020 ERC CoG 2015 AROMA-CFD project 681447 that supported the development of multiphenics.

Supplementary material

Supplementary material associated with this article can be found, in the online version, at doi:10.1016/j.advwatres.2020.103620.

References

Alnaes, M., Blechta, J., Hake, J., Johansson, A., Kehlet, B., Logg, A., Richardson, C., Ring, J., Rognes, M., Wells, G., 2015. The FEniCS project version 1.5. Arch. Numer. Softw. 3 (100). https://doi.org/10.11588/ans.2015.100.20553.

Andrianov, N., Nick, H., 2019. Modeling of waterflood efficiency using outcrop-based fractured models. J. Pet. Sci. Eng. 183, 106350.

Angot, P., Boyer, F., Hubert, F., 2009. Asymptotic and numerical modelling of flows in fractured porous media. ESAIM Math. Model. Numer.Anal. 43 (2), 239–275.

Antonietti, P., Facciola, C., Russo, A., Verani, M., 2019. Discontinuous Galerkin approximation of flows in fractured porous media on polytopic grids. SIAM J. Sci. Comput. 41 (1), A109–A138.

Arnold, D., Brezzi, F., Cockburn, B., Marini, L., 2002. Unified analysis of discontinuous Galerkin methods for elliptic problems. SIAM J. Numer. Anal. 39 (5), 1749–1779.

Babuska, I., 1973. The finite element method with lagrangian multipliers. Numer. Math. 20 (3), 179–192.

Ballarin, F., Rozza, G., 2019. multiphenics - easy prototyping of multiphysics problems in FEniCS.

Berre, I., Boon, W., Flemisch, B., Fumagalli, A., Glaser, D., Keilegavlen, E., Scotti, A., Stefansson, I., Tatomir, A., Brenner, K., et al., 2020. Verification benchmarks for single-phase flow in three-dimensional fractured porous media. arXiv:2002.07005.

Berrone, S., Fidelibus, C., Pieraccini, S., Scialo, S., Vicini, F., 2018. Unsteady advection-diffusion simulations in complex discrete fracture networks with an optimization approach. J. Hydrol. 566, 332–345.

Bisdom, K., Bertotti, G., Nick, H., 2016. A geometrically based method for predicting stress-induced fracture aperture and flow in discrete fracture networks. Am. Assoc. Pet. Geol. Bull. 100 (7), 1075–1097.

Boon, W., Nordbotten, J., Yotov, I., 2018. Robust discretization of flow in fractured porous media. SIAM J. Numer. Anal. 56 (4), 2203–2233.

Chave, F., Di Pietro, D., Formaggia, L., 2018. A hybrid high-order method for darcy flows in fractured porous media. SIAM J. Sci. Comput. 40 (2), A1063–A1094.

Chen, Z., Huan, G., Ma, Y., 2006. Computational Methods for Multiphase Flows in Porous Media, vol. 2. Siam.

Choo, J., Lee, S., 2018. Enriched Galerkin finite elements for coupled poromechanics with local mass conservation. Comput. Methods Appl. Mech. Eng. 341, 311–332.

De Dreuzy, J., Pichot, G., Poirriez, B., Erhel, J., 2013. Synthetic benchmark for modeling flow in 3d fractured media. Comput. Geosci. 50, 59–71.

D'Angelo, C., Scotti, A., 2012. A mixed finite element method for darcy flow in fractured porous media with non-matching grids. ESAIM Math. Model. Numer.Anal. 46 (2), 465–489.

Flemisch, B., Berre, I., Boon, W., Fumagalli, A., Schwenck, N., Scotti, A., Stefansson, I., Tatomir, A., 2018. Benchmarks for single-phase flow in fractured porous media. Adv. Water Resour. 111, 239–258.

Flemisch, B., Fumagalli, A., Scotti, A., 2016. A review of the XFEM-based approximation of flow in fractured porous media. In: Advances in Discretization Methods. Springer, pp. 47–76.

Flemisch, B., Helmig, R., 2008. Numerical investigation of a mimetic finite difference method. In: Finite Volumes for Complex Applications V–Problems and Perspectives, pp. 815–824.

Formaggia, L., Scotti, A., Sottocasa, F., 2018. Analysis of a mimetic finite difference approximation of flows in fractured porous media. ESAIM Math. Model. Numer.Anal. 52 (2), 595–630.

Fumagalli, A., Keilegavlen, E., Scialo, S., 2019. Conforming, non-conforming and non–matching discretization couplings in discrete fracture network simulations. J. Comput. Phys. 376, 694–712.

Geiger, S., Dentz, M., Neuweiler, I., et al., 2013. A novel multi-rate dual-porosity model for improved simulation of fractured and multiporosity reservoirs. SPE J. 18 (4), 670–684.

Glaser, D., Flemisch, B., Helmig, R., Class, H., 2019. A hybrid-dimensional discrete fracture model for non-isothermal two-phase flow in fractured porous media. GEM Int. J. Geomath. 10 (1), 5.

Glaser, D., Helmig, R., Flemisch, B., Class, H., 2017. A discrete fracture model for two-phase flow in fractured porous media. Adv. Water Resour. 110, 335–348.

Hajibeygi, H., Karvounis, D., Jenny, P., 2011. A hierarchical fracture model for the iterative multiscale finite volume method. J. Comput. Phys. 230 (24), 8729–8743.

Hoteit, H., Firoozabadi, A., 2008. Numerical modeling of two-phase flow in heterogeneous permeable media with different capillarity pressures. Adv. Water Resour. 31 (1), 56–73.

Jia, P., Cheng, L., Huang, S., Xu, Z., Xue, Y., Cao, R., Ding, G., 2017. A comprehensive model combining laplace-transform finite-difference and boundary-element method for the flow behavior of a two-zone system with discrete fracture network. J. Hydrol. 551, 453–469.

Jones, E., Oliphant, T., Peterson, P., Others, 2001. SciPy: Open source scientific tools for Python.

Juanes, R., Samper, J., Molinero, J., 2002. A general and efficient formulation of fractures and boundary conditions in the finite element method. Int. J. Numer. Methods Eng. 54 (12), 1751–1774.

Kadeethum, T., Jörgensen, T., Nick, H., 2020. Physics-informed neural networks for solving nonlinear diffusivity and biots equations. PLoS ONE 15 (5), e0232683.

Kadeethum, T., Nick, H., Lee, S., 2019. Comparison of two-and three-field formulation discretizations for flow and solid deformation in heterogeneous porous media. In: 20th Annual Conference of the International Association for Mathematical Geosciences, PA, USA.

Kadeethum, T., Nick, H., Lee, S., Ballarin, F., 2020b. Enriched Galerkin discretization for modelling poroelasticity and permeability alteration in heterogeneous porous media. In revision.

Kadeethum, T., Nick, H., Lee, S., Richardson, C., Salimzadeh, S., Ballarin, F., 2019. A novel enriched Galerkin method for modelling coupled flow and mechanical deformation in heterogeneous porous media. 53rd US Rock Mechanics/Geomechanics Symposium. American Rock Mechanics Association, New York, NY, USA.

Kadeethum, T., Salimzadeh, S., Nick, H., 2019. An investigation of hydromechanical effect on well productivity in fractured porous media using full factorial experimental design. J. Pet. Sci. Eng. 181, 106233.

Kadeethum, T., Salimzadeh, S., Nick, H., 2020. Well productivity evaluation in deformable single-fracture media. Geothermics 87.

Karimi-Fard, M., Durlofsky, L., Aziz, K., et al., 2004. An efficient discrete-fracture model applicable for general-purpose reservoir simulators. SPE J. 9 (2), 227–236.

Keilegavlen, E., Fumagalli, A., Berge, R., Stefansson, I., Berre, I., 2017. PorePy: an open-source simulation tool for flow and transport in deformable fractured rocks. arXiv:1712.00460.

Khoei, A., Vahab, M., Hirmand, M., 2018. An enriched–FEM technique for numerical simulation of interacting discontinuities in naturally fractured porous media. Comput. Methods Appl. Mech. Eng. 331, 197–231.

Latham, J., Lei, Q., Obeysekara, A., Yang, P., Xiang, J., Salinas, P., Pain, C., 2018. Recent advances in hydromechanical modelling of fractured rocks using the finite-discrete element method. In: International Conference on Coupled Processes in Fractured Geological Media, CouFrac.

Latham, J., Xiang, J., Belayneh, M., Nick, H., Tsang, C., Blunt, M., 2013. Modelling stress-dependent permeability in fractured rock including effects of propagating and bending fractures. Int. J. Rock Mech. Min. Sci. 57, 100–112.

Lee, S., Kadeethum, T., Nick, H., 2019. Choice of interior penalty coefficient for interior penalty discontinuous Galerkin method for Biot's system by employing machine learning. Submitted.

Lee, S., Lee, Y., Wheeler, M., 2016. A locally conservative enriched Galerkin approximation and efficient solver for elliptic and parabolic problems. SIAM J. Sci. Comput. 38 (3), A1404–A1429.
Lee, S., Mikelic, A., Wheeler, M., Wick, T., 2016. Phase-field modeling of proppant-filled fractures in a poroelastic medium. Comput. Methods Appl. Mech. Eng. 312, 509–541.
Lee, S., Mikelic, A., Wheeler, M., Wick, T., 2018. Phase-field modeling of two phase fluid filled fractures in a poroelastic medium. Multiscale Model. Simul. 16 (4), 1542–1580.
Lee, S., Wheeler, M., 2017. Adaptive enriched Galerkin methods for miscible displacement problems with entropy residual stabilization. J. Comput. Phys. 331, 19–37.
Lee, S., Wheeler, M., 2018. Enriched Galerkin methods for two-phase flow in porous media with capillary pressure. J. Comput. Phys. 367, 65–86.
Martin, V., Jaffre, J., Roberts, J., 2005. Modeling fractures and barriers as interfaces for flow in porous media. SIAM J. Sci. Comput. 26 (5), 1667–1691.
Matthai, S., Nick, H., 2009. Upscaling two-phase flow in naturally fractured reservoirs. Am. Assoc. Pet. Geol. Bull. 93 (11), 1621–1632.
Matthai, S., Nick, H., Pain, C., Neuweiler, I., 2010. Simulation of solute transport through fractured rock: a higher-order accurate finite-element finite-volume method permitting large time steps. Transp. Porous Media 83 (2), 289–318.
Nick, H., Matthai, S., 2011. Comparison of three FE-FV numerical schemes for single-and two-phase flow simulation of fractured porous media. Transp. Porous Media 90 (2), 421–444.
Nick, H., Matthai, S., 2011. A hybrid finite-element finite-volume method with embedded discontinuities for solute transport in heterogeneous media. V. Zone J. 10 (1), 299–312.
Obeysekara, A., Lei, Q., Salinas, P., Pavlidis, D., Xiang, J., Latham, J., Pain, C., 2018. Modelling stress-dependent single and multi-phase flows in fractured porous media based on an immersed-body method with mesh adaptivity. Comput. Geotech. 103, 229–241.
Odsaeter, L., Kvamsdal, T., Larson, M., 2019. A simple embedded discrete fracture–matrix model for a coupled flow and transport problem in porous media. Comput. Methods Appl. Mech. Eng. 343, 572–601.
Peng, S., Zhang, Z., Li, C., He, G., Miao, G., 2017. Simulation of water flow in fractured porous medium by using discretized virtual internal bond. J. Hydrol. 555, 851–868.
Prevost, J., Sukumar, N., 2016. Faults simulations for three-dimensional reservoir-geomechanical models with the extended finite element method. J. Mech. Phys. Solids 86, 1–18.
Rinaldi, A., Rutqvist, J., 2019. Joint opening or hydroshearing? Analyzing a fracture zone stimulation at Fenton Hill. Geothermics 77, 83–98.
Rivie, B., Wheeler, M., Banas, K., et al., 2000. Part ii. Discontinuous Galerkin method applied to a single phase flow in porous media. Comput. Geosci. 4 (4), 337–349.
Riviere, B., 2008. Discontinuous Galerkin Methods for Solving Elliptic and Parabolic Equations: Theory and Implementation. SIAM.
Ruiz Baier, R., Gizzi, A., Loppini, A., Cherubini, C., Filippi, S., 2019. Modelling thermo–electro-mechanical effects in orthotropic cardiac tissue. Commun. Comput. Phys..
Salimzadeh, S., Grandahl, M., Medetbekova, M., Nick, H., 2019. A novel radial jet drilling stimulation technique for enhancing heat recovery from fractured geothermal reservoirs. Renew. Energy 139, 395–409.
Salimzadeh, S., Hagerup, E., Kadeethum, T., Nick, H., 2019. The effect of stress distribution on the shape and direction of hydraulic fractures in layered media. Eng. Fract. Mech. 215, 151–163.
Salimzadeh, S., Khalili, N., 2015. Three-dimensional numerical model for double-porosity media with two miscible fluids including geomechanical response. Int. J. Geomech. 16 (3).
Salimzadeh, S., Nick, H., 2019. A coupled model for reactive flow through deformable fractures in enhanced geothermal systems. Geothermics 81, 88–100.
Salimzadeh, S., Paluszny, A., Zimmerman, R., 2018. Effect of cold CO2 injection on fracture apertures and growth. Int. J. Greenhouse Gas Control 74, 130–141.
Salinas, P., Pavlidis, D., Xie, Z., Osman, H., Pain, C., Jackson, M., 2018. A discontinuous control volume finite element method for multi-phase flow in heterogeneous porous media. J. Comput. Phys. 352, 602–614.
Sanborn, S., Prevost, J., 2011. Frictional slip plane growth by localization detection and the extended finite element method (XFEM). Int. J. Numer. Anal. Methods Geomech. 35 (11), 1278–1298.
Santillan, D., Juanes, R., Cueto-Felgueroso, L., 2018. Phase field model of hydraulic fracturing in poroelastic media: fracture propagation, arrest, and branching under fluid injection and extraction. J. Geophys. Res. 123 (3), 2127–2155.
Scovazzi, G., Wheeler, M., Mikelic, A., Lee, S., 2017. Analytical and variational numerical methods for unstable miscible displacement flows in porous media. J. Comput. Phys. 335, 444–496.
Secchi, S., Schrefler, B., 2012. A method for 3-d hydraulic fracturing simulation. Int. J. Fract. 178 (1–2), 245–258.
Segura, J., Carol, I., 2008. Coupled HM analysis using zero-thickness interface elements with double nodes. Part i: theoretical model. Int. J. Numer. Anal. Methods Geomech. 32 (18), 2083–2101.
Stefansson, I., Berre, I., Keilegavlen, E., 2018. Finite-volume discretisations for flow in fractured porous media. Transp. Porous Media 124 (2), 439–462.
Sun, S., Liu, J., 2009. A locally conservative finite element method based on piecewise constant enrichment of the continuous Galerkin method. SIAM J. Sci. Comput. 31 (4), 2528–2548.
Vinje, V., Brucker, J., Rognes, M., Mardal, K., Haughton, V., 2018. Fluid dynamics in syringomyelia cavities: effects of heart rate, CSF velocity, CSF velocity waveform and craniovertebral decompression. Neuroradiol J. 31 (5), 482–489.
Wheeler, M., Srinivasan, S., Lee, S., Singh, M., et al., 2019. Unconventional reservoir management modeling coupling diffusive zone/phase field fracture modeling and fracture probability maps. In: SPE Reservoir Simulation Conference. Society of Petroleum Engineers.
Wheeler, M., Xue, G., Yotov, I., 2012. A multipoint flux mixed finite element method on distorted quadrilaterals and hexahedra. Numer. Math. 121 (1), 165–204.
Willems, C., Nick, H., 2019. Towards optimisation of geothermal heat recovery: an example from the west netherlands basin. Appl. Energy 247, 582–593.
Zhang, Q., Lin, S., Xie, Z., Su, H., 2016. Fractured porous medium flow analysis using numerical manifold method with independent covers. J. Hydrol. 542, 790–808.
Zi, G., Song, J., Budyn, E., Lee, S., Belytschko, T., 2004. A method for growing multiple cracks without remeshing and its application to fatigue crack growth. Modell. Simul. Mater. Sci. Eng. 12 (5), 901.